universität wien

MASTERARBEIT / MASTER'S THESIS

Titel der Masterarbeit / Title of the Master's Thesis

„Characterization of CdZnTe detectors“

verfasst von / submitted by

Constanze Leeb, BSc BA

angestrebter akademischer Grad / in partial fulfilment of the requirements for the degree of

Master of Science (MSc)

Wien, 2021 / Vienna, 2021

Studienkennzahl lt. Studienblatt / degree programme code as it appears on the student record sheet:	A 066 876
Studienrichtung lt. Studienblatt / degree programme as it appears on the student record sheet:	Masterstudium Physik
Betreut von / Supervisor:	Priv.-Doz. Dr. Johann Zmeskal

Abstract

Cadmium-Zinc-Telluride (CdZnTe) detectors are semiconductor-based radiation detectors. They are sensitive to X-ray and γ-ray events within a broad energy range. Applications of interest not only include hadron- or astrophysics, but further medicine, as they are operable at room temperature without the need for cooling. This is due to their large band gap of 1.5 - 1.6 eV, in comparison to Silicium or Germanium, which have smaller band gaps and are often used for detection. In addition, the higher atomic numbers of CdZnTe result in a higher detection efficiency.

Due to these desirable aspects, the HORIZON 2020 project ASTRA was launched, focusing on developing CdZnTe detectors and customized read-out electronics. Two detectors have been tested and characterized at the Stefan Meyer Institute for Subatomic Physics. They each consist of a cathode, an anode and a guard ring, but differ in their thickness and the guard ring area. Testing included investigation of the current-voltage relationship and the usage of different pre-amplifiers. Both the cathode and the anode were biased. In addition, the guard ring of the detectors was biased for some measurements as well. An energy calibration and measurements with various foils were performed. Some of the mentioned measurements were also performed with an industry-manufactured detector for comparison. For this, the Ritec CZT/500 was used. These measurements are presented and discussed in this thesis.

Zusammenfassung

Cadmium-Zink-Tellurid (CdZnTe) Detektoren bestehen aus Halbleitermaterialien und sind über einen breiten Energiebereich sensitiv auf Röntgen- und Gammastrahlung. Sie kommen in der Hadronen- und Astrophysik zum Einsatz, finden jedoch auch Anwendungsbereiche in der Medizin. Sie sind für dieses Feld besonders attraktiv, da sie auch bei Raumtemperatur einsetzbar sind ohne gekühlt werden zu müssen. Hierfür ist ihre Bandlücke verantwortlich, die mit 1.5 - 1.6 eV deutlich größer ist als jene von Silizium oder Germanium, andere Halbleitermaterialien die häufig zum Einsatz kommen. Zusätzlich sind die hohen Ordnungszahlen des Materials ein Vorteil, da sie zu einer höheren Detektionsrate führen.
Auf Grund dieser Eigenschaften wurde das HORIZON 2020 Projekt ASTRA gestartet, welches sich mit der Entwicklung von CdZnTe-Detektoren und der nötigen Elektronik zum Auslesen der Signale beschäftigt. Zwei Detektoren wurden am Stefan Meyer Institut für Subatomare Physik getested und charakterisiert. Beide Detektoren bestehen aus einer Kathode, einer Anode und einem Guardring. Sie unterscheiden sich in der Fläche die der Guardring einnimmt und ihrer Dicke. Die Testungen beinhalteten das Untersuchen von Strom-Spannungskennlinien und die Verwendung von zwei verschiedenen Vorverstärkern. Die Kathode und die Anode wurden gebiased. Zusätzlich wurde der Guardring für manche Messungen auch gebiased. Eine Energiekalibrierung und Messungen mit verschiedensten Materialfolien waren ebenso Teil der Charakterisierung. Manche dieser Messungen wurden zusätzlich mit einem industriell hergestellten Detektor durchgeführt, um die Resultate vergleichen zu können. Dafür wurde der RITEC CZT/500 verwendet. Die Messungen werden in der folgenden Arbeit präsentiert und diskutiert.

Acknowledgments

Firstly, I want to mention Hannes, my supervisor, without whom this thesis would not exist. More importantly, he showed me the amazing field of experimental physics in the lab. I want to thank him for sharing not only his knowledge and expertise with me, but also his passion and excitement. Without him I would never have found my own passion for experimental lab work. In addition, I want to thank Eberhard for giving me the opportunity to do hands-on research during all my university stages by being part of the SMI. I also want to thank our research partners of the ASTRA project.

The people who made coming to the lab every single day especially joyful are my incredible colleagues. Thank you Julia, Doris and Fiona for all the laughters, amazing events and for making the SMI-Team so incredible. To my CERN-labeling-partners, Alina and Andi, thank you for always being the spot in the downstairs lab that one wanted to visit. Amit, thank you for being this spot in the third floor and for all the shared ice cream. I want to thank Herbert, Gerhard, Sebastian, Leo and Mark for always helping and supporting me, no matter how much else they had to do.

My time at SMI would not be complete without Vici and Marlene. Vici, thank you for all the fun we had together in the many hours doing university work together, no matter what time of the day (or night) or level of frustration we had. Marlene, thank you for being my big sister in research and sharing your amazingly organized working methods in the lab (I would not have survived without them). Both of you, thank you for the unforgettable and best moments I had at SMI. Thank you for all the tears of laughter, the hours of listening to music in the lab together and being there for each other, no matter if for holding a vacuum chamber in place or constructing 96 double-wounded cables. Most importantly, thank you for being such incredible friends.

Kristina, Helene and Viki, thank you for always helping me out and for the amazing working atmosphere we shared. Daniela, Jolly, Ela, Mara and Bella, no matter how far apart, thanks for always having an open ear and being there in every part of my journey. Veronika, Viki and Ruth, thank you for many good memories, in the lecture halls and outside.

Thanks to the person who is not only the reason why I have trouble spelling “manual” correctly, but who really is true to his name with his constant support and incredible ability in sharing knowledge. Manu, thank you for the best pep-talks, for making me laugh and that I can always count on you.

Lastly, I want to thank my family for their constant support. Thanks to my parents, who have taught me how wonderful it is to be curious and who always believe in me and are proud, no matter what path I take. Thanks to my two big sisters for being amazing role models and friends and thanks to them and my brothers in law for always supporting me.

Contents

1 Introduction

Within the European Union program Horizon 2020, the project STRONG 2020 received funding to investigate "the strong interaction at the frontier of knowledge" [1]. This includes both fundamental research and a focus on applications in order to answer some of the still open questions concerning one of the fundamental forces, the strong interaction. The studied frontiers can be divided into four areas looking respectively at low energy, high energy, infrastructures and instrumentation. Each one of them consists of several work packages, one of them being the package JRA8-ASTRA. It is part of the instrumentation sector [1] and the acronym stands for Advanced ultra-fast solid STate detectors for high precision RAdiation spectroscopy (ASTRA) [2].

Aim of ASTRA is the development of two different kinds of semiconductor-based radiation detectors, namely Cadmium Telluride (CT or CdTe) and Cadmium Zinc Telluride (CZT or CdZnTe), and customized read-out electronics. CdTe will be optimized for lower energies, CdZnTe for higher energy ranges [2]. This thesis will focus on the latter one. The international collaboration of ASTRA consists of researchers from institutions from different countries, namely *ÖAW, Stefan Meyer Institute, Austria* (the home institute of the author); *Istituto Materiali per Elettronica e Magnetismo, CNR, Parma, Italy*; *Jagiellonian University, Krakow, Poland*; *Laboratori Nazionali di Frascati - INFN, Italy*; *University of Zagreb, Croatia*; *Politecnico Milano, Dipartimento di Elettronica, Italy* [2].
The detectors are required to be sensitive to X-ray and γ-ray events in a broad energy range from a few keV up to MeV and to yield high-precision measurements. The goal is an ultra-fast radiation detector system with timing capabilities of a few ns that approaches the theoretical limits of the Full Width at Half Maximum (FWHM) of around 200 eV at 10 keV and 610 eV at 100 keV [2]. Applications of these detectors include not only the field of hadron physics. They are already used in Astrophysics, for example as part of the IBIS detector on board of ESA's INTEGRAL [3], as well as in medical applications, for example in portable systems for mammography [4].

2 CdZnTe

This thesis focuses on one of the detectors developed within the framework of the ASTRA project (see chapter 1): Cadmium Zinc Telluride, which will just be called CdZnTe in the following sections.

2.1 Specifications

CdZnTe has a high density of around 5.81 $\frac{g}{cm^3}$ [3] and is a ternary [4] semiconductor material with a cubic, zincblende-type lattice [4] that consists of the elements Cadmium (Cd), Zinc (Zn) and Tellurium (Te) [5]. Other semiconductor materials often used are Silicium (Si) and Germanium (Ge). One of the advantages of CdZnTe is that all the used elements have high atomic numbers, namely 48 (Cd), 30 (Zn) and 52 (Te) compared to Si with an atomic number of only 14 [6].
The ratio between the number of photons detected by the detector and the incident number of photons is called detection efficiency [7]. As the probability of an interaction (photoelectric effect, compton scattering or pair production) of the photon scales with Atomic number (Z) of the material ($Z^{4.5}$ for the photoelectric effect, Z for compton scattering and Z^2 for pair production), CdZnTe has a higher interaction cross section than Si [4]. This leads to a higher detection efficiency of CdZnTe. As can be seen in figure 2.1, the detection of 100 keV γ-ray photons is noticeably better for CdTe and CdZnTe than for Ge or Si and increases with the thickness of the detector [3]. However, it should be pointed out that the figure is based on calculations that assume that the photons deposit all of their energy in the detector and that no electron-hole pairs are lost. The charge loss within CdTe and CdZnTe does reduce this efficiency greatly [3] and limits its thickness as well (see section 2.2).

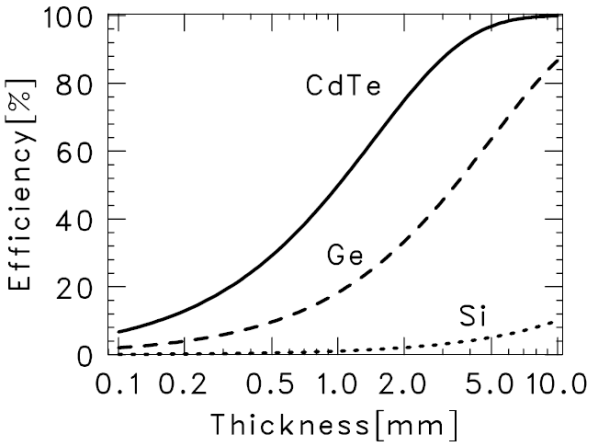

Figure 2.1: Detection efficiency for 100 keV γ-ray photon in various thickness of CdTe (and also CdZnTe), Si and Ge (taken from [3], p.2).

In addition, CdZnTe has a larger band gap than Si or Ge. Solid state materials consist of (energy) bands which are separated by band gaps. These bands can be filled with electrons, depending on the energies of these electrons. The highest band in terms of energy that is filled is called the valence band, the lowest unfilled band is the conduction band. When speaking about the band gap, one refers to the energy gap between the valence and the conduction band, illustrated in figure 2.2. If the gap is rather small, thermal fluctuations can be enough to excite an electron in the valence band into the conduction band [8]. In detectors, this is not a desired property, as the electrons should only move into the conduction band when being excited by an incoming particle. Therefore, the larger band gap of CdZnTe, which is around 1.5 to 1.6 eV ([4],[3]), depending on the exact composition of the material [4], is an advantage compared to the lower band gaps of Si with 1.12 eV and Ge with 0.66 eV (at 300 K for all values) [9]. This semi-insulating material [3] allows operation of the detector at room temperature [2], making it attractive for many applications.

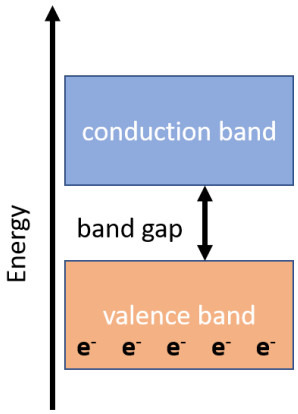

Figure 2.2: Scheme of the valence and the conduction band with a band gap between them.

The CdZnTe is proposed to be sensitive in the energy range of 0.05 to 1 MeV. For a Cadmium Zinc Telluride of 5 mm thickness an intrinsic efficiency of 25% at 511 keV is expected [2]. While the energy resolution is worse than for Si or Ge, the timing and resistance for high rates is better for CdZnTe [2].

2.2 Functionality

The working principle of a Cadmium Zinc Telluride could be summarized as a "solid ionization chamber" ([3], p.3). Incident radiation will interact with the material and activate the atoms to produce electron-hole pairs [10] which are proportional in number to the energy of the incoming photon. By applying a bias voltage to the detector, the electrons can be collected and measured. Figure 2.3 shows the simplest configuration of a CdZnTe, the planar configuration. The cathode (the negative electrode) is located on one side, the anode (the positive electrode) can be found on the opposite.

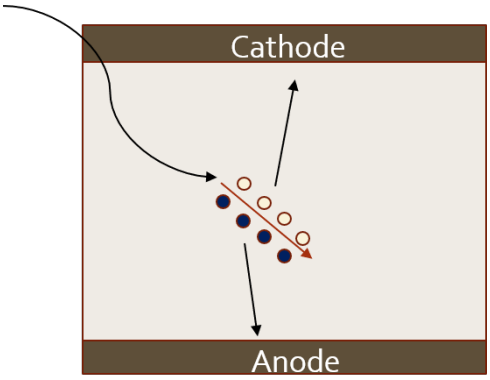

Figure 2.3: Planar configuration of a CdZnTe. Filled circles represent electrons and open circles holes.

When a bias voltage is introduced, it creates an electrical field between these electrodes. If an electron-hole pair is created by an incoming photon, the negatively charged electron will travel towards the positive anode, while the hole will move towards the cathode. However, they do so with different velocities. Holes have a lower mobility and shorter lifetime than electrons. When a hole is drifting towards the cathode, it might recombine with other electrons due to its slow movement and alter the resulting signal. Therefore, the detector thickness should be smaller than the mean drift path of the slower charge carrier, which can be estimated using the product of the mobility μ, the lifetime τ and the electric field E. This yields the following limitation for the detector thickness l, in order to reduce hole trapping [3]:

$$l < \mu\tau E. \tag{2.1}$$

In addition, it is helpful to place the radioactive source on the cathode during experiments [3]. The electron-hole pairs will more likely be created close to the negative electrode and the path

for the hole will be as short as possible. Therefore, a recombination of a hole with an electron becomes less likely.

The voltage applied creates a weighting potential in the detector which can be defined as "the potential that would exist in the detector with the collecting electrode held at unit potential, while holding all other electrodes at zero potential" ([4], p.3494). It can be calculated by solving the Laplace equation inside the CdZnTe [4]. Following the Shockley-Ramo theorem, a particle inducing charge at the electrode is proportional to the weighting potential at this electrode [11]. The weighting potential is lower close to the cathode and then starts rising towards the anode [12], enabling a good charge collection efficiency as hole signals can be neglected [11]. The weighting potential highly depends on the configuration of the detector (see section 2.4).

Due to the properties of the energy bands in a solid state material (see section 2.1), the performance of CdTe [10] and CdZnTe is temperature dependent. The spectral performance improves by cooling down, as the noise can be reduced. Below a certain temperature the resolution worsens due to perturbations of the electrical field which happen through formations of accumulations of positive charges. These slow the charges down and the low temperature further inhibits the disentangling process [12].

2.3 Production

There can be different alloy mixtures of CdTe and ZnTe that make up a solid solution. This can be described through the formula $Cd_{1-x}Zn_xTe$, with x being the blending fraction of ZnTe in CdTe [4]. The values for x range between 0.08 and 0.2 [3], [4] and influence the properties of the resulting CdZnTe. An example is the larger band gap when increasing the abundance of Zn [3]. This can be relevant, as the larger band gap yields a high electrical resistivity, therefore a low leakage current and good electron transportation, leading to an improved spectral performance [3] and the possibility to apply a higher bias voltage [4].
There exist different CdZnTe production methods, but a common factor is usually that they are being produced with ohmic contacts consisting of Platinum (Pl) or Gold (Au) [4].

Production methods include the High-Pressure Bridgman (HPB) method, Vertical Bridgman and Low-Pressure Bridgman method, all of which are based on the Bridgman technique [4]. Figure 2.4 shows the temperature gradient profile and the basic set up of the method. A polycrystalline material is melted in a hot zone in a crucible. Then it is brought in contact with a single-crystal seed which will start melting as well. The crucible will be moved downwards (or to the side [13] in the simpler [14] vertical version, see figure 2.4) into a cold zone, ensuring that the crystal growth is initiated by the seed at the bottom of the crucible. Finally, the whole crucible will be moved into the cooler zone and the development into a solid crystalline

will start [13]. In commercial production, the HPB method is the most commonly used one. For High-Pressure Bridgman, the Bridgman technique described above is used and a gas (often Argon) is kept at over-pressure to keep the melted material from evaporating [15]. However, it can only yield polycrystals which have the disadvantage of non-uniform distributions of $\mu\tau$ (mobility times lifetime) within the detector [3]. Often, undesired crucible-crystal interactions take place [4]. In addition, larger areas above 10x10 mm^2 are the limit for this method [3].

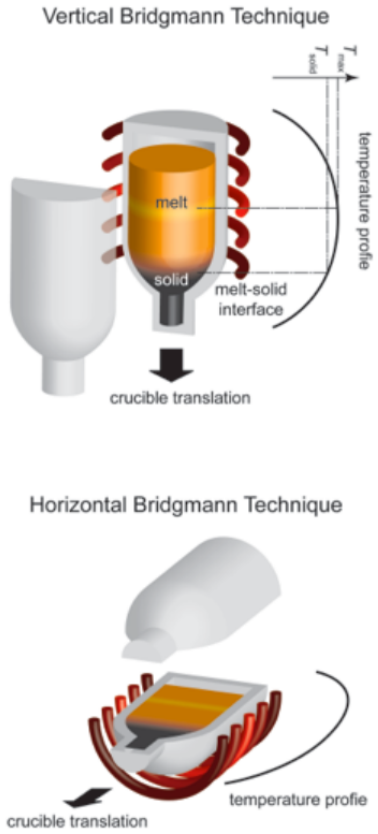

Figure 2.4: Horizontal and Vertical Bridgman method (taken from [13]).

A special technique based on the Vertical Bridgman technique is the so called Boron Oxide Encapsulated Vertical Bridgman technique which is shortly described as two samples used for this thesis were produced with this method (namely Sample A and Sample B) [2]. Three separate temperature zones exist in the set up. Directly above the polycrystalline CdZnTe material (which is in a quartz crucible) a boron oxide pellet is placed as can be seen in figure 2.5. The temperature is increased, the boron oxide starts melting first and then the whole crucible is moved further into the hotter zones. The growth starts without any seeding. In the end the newly formed crystal is put into water. As an effect of the water, the boron oxide expands and breaks the crucible walls, leaving a single crystal without any interactions with the crucible [4].

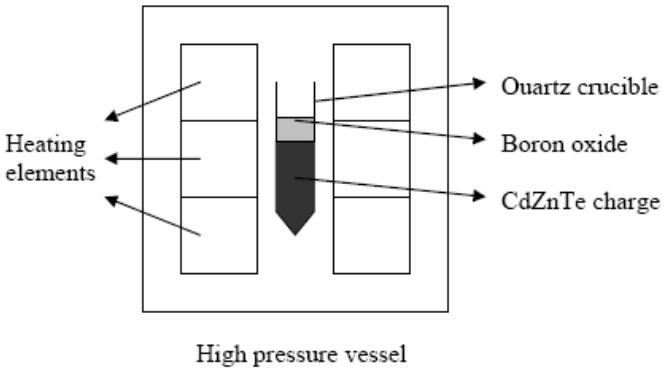

Figure 2.5: Boron Oxide Encapsulated Vertical Bridgman technique (taken from [4], p.3503).

2.4 Different configurations

In figure 2.3 in section 2.2 the most basic configuration of CdZnTe is shown, consisting of an anode on one side and a cathode on the opposite side of the detector. Besides this planar structure, various configurations can be implemented.

2.4.1 Guard rings

It is possible to include a guard ring, a grounded contact, around the anode (or anode pixels). Its purpose is the reduction of electronic noise as it ensures that surface currents will not be collected by the anode. Nevertheless, charge sharing can happen with the guard ring [11] in the same way as with neighbouring pixels, which will be discussed in subsection 2.4.2.

The introduction of a guard ring compresses the weighting potential towards the anode. The size of the anode within a guard ring plays an important role as it highly influences the weighting potential. In this paper [5] simulate the weighting potentials for different configurations based on the Frisch-grid technique (see below in subsection 2.4.3 for more information) using the finite element method. Here, the role of the anode size and the guard ring becomes more evident. In figure 2.6 two different models are shown. Model C has a small guard ring and Model D has a large guard ring (names of the models are taken from [5]). In the case of Model C the weighting potential starts to rise again when moving away from the anode if the area of the anode is too large (see figure 2.6 (b)). However, if the guard ring covers the rest of the detector area as in Model D, the weighting potential will act in a stable way (see figure 2.6 (c)) [5].

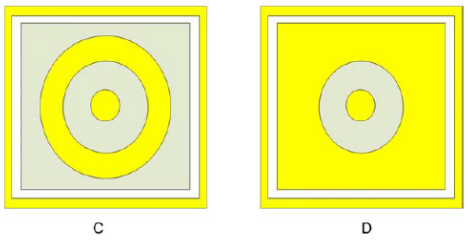

(a) Model C and Model D.

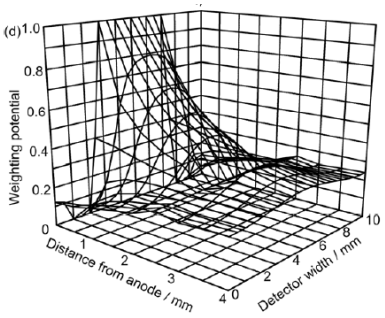

(b) Weighting potential for Model C (anode radius = 2 mm).

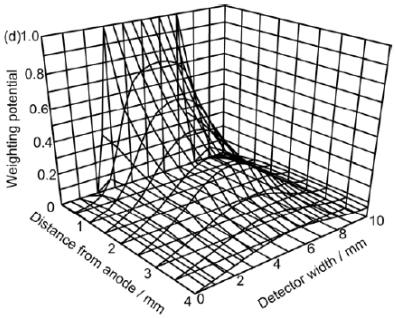

(c) Weighting potential for Model D (anode radius = 2 mm).

Figure 2.6: The small yellow circle in both plots in the middle indicates the anode. The other yellow area is the guard ring. (a) shows Model C (smaller guard ring) and Model D (guard ring covering rest of the detector surface) with (b), (c) the weighting potentials (taken from [5], p.47 & 49).

2.4.2 Pixel/Strips detectors

CdZnTe pixel detectors have an anode that consists of small pixel areas [12], as can be seen in figure 2.7. One advantage of this configuration is the possibility of adjusting the gain for each pixel separately, compensating inhomogeneities of the material [11]. Apart from the improved spatial resolution, the weighting potential will be focused under the pixel in a small region, taking advantage of the so-called "small pixel effect", which becomes especially desirable if thicker detectors are produced. As the weighting potential depends on the configuration of the detector and its electrodes, the reduction in the size of the electrodes improves the weighting potential drastically [11]. Disadvantages include the higher number of needed read-out channels [11], charge sharing and crosstalk among the pixels, the loss of charge between the pixels [12] and the more difficult process of bonding them to the crystal [11]. One speaks of crosstalk when the charge collected by one pixel induces a charge collection by the neighbouring pixel. Charge sharing happens if a charge cloud, which has been produced by a single photon, generates a signal in neighbouring pixels [12]. The phenomenon of charge sharing becomes especially critical for thicker detectors. Charge clouds have more time until they reach the electrodes to spread across

the pixels due to repulsion and diffusion. However, this can be accounted for through temporal coincidence measurements of the pixels [11]. The advantages and disadvantages stated above also hold for a strip anode structure [4].

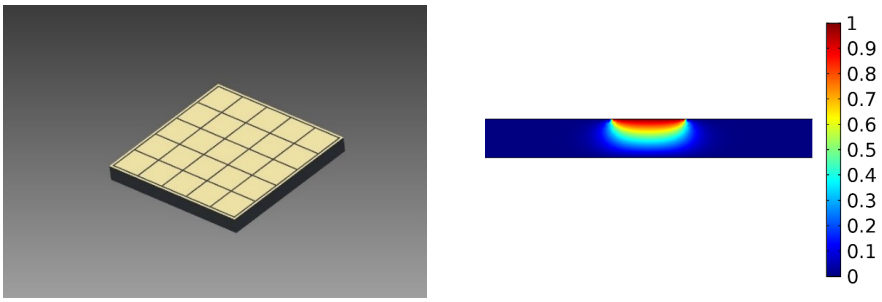

Figure 2.7: Model and weighting potential of an anode structure with pixels in a 5x5 matrix enclosed by a guard ring (taken from [11], p.3).

2.4.3 Frisch-grid technique

The Frisch-grid configuration gives a solution to trying to have large enough pixels to reduce charge sharing while still not loosing the "small pixel effect". In this structure, a non-collecting contact surrounds the whole crystal on its sides, as can be seen in figure 2.8. To realize such a structure, the dimension of the thickness must be greater than the other two dimensions. Crystal inhomogeneities can also be addressed as the signal on the sides of the detector can point to the interaction position. However, the production process of Frisch-grid configurations is more complicated than for pixel structures [11].

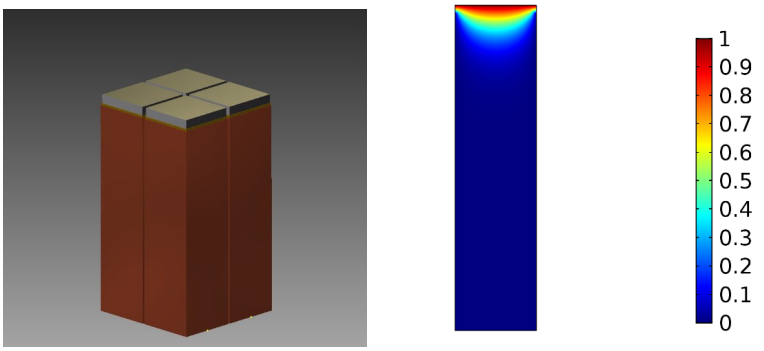

Figure 2.8: 3D model of the Frisch-grid configuration with non-collecting electrodes (red) and the weighting potential (taken from [11], p.6).

2.4.4 Hemispherical geometry

In this geometry, the detector has a hemispherical shape with the positive electrode (the anode) at the center of the flat part. The spherical surface on the outside is grounded. With voltage applied, the electrical field will be especially strong at the anode due to its radial shape.

In figure 2.9 the hemispherical geometry of a detector is shown. It can be seen that the electrons travel to the anode and the holes to the grounded spherical surface. The hatched region is the lower field region which makes up the majority of the detector volume and therefore contributes to a large amount of the detected charge [16].

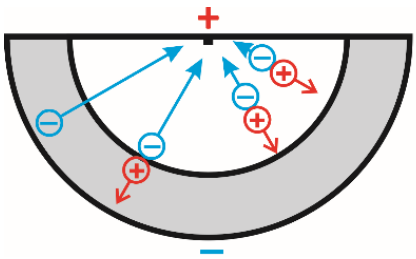

Figure 2.9: The hemispherical geometry of the CZT/500 detector produced by RITEC (taken from [16], p.7).

3 The three samples used

For this thesis, three different samples of CdZnTe were used. They will be introduced in the following sections.

3.1 Sample A & Sample B

Sample A and Sample B are attached to two small PCB boards (the dimensions of the boards are 25x12 mm2 with a thickness of 1 mm). To reduce noise, the material DiClad was used for the boards [17]. The layout of the PCB boards can be seen in figure 3.1, showing the top, side and bottom view with the important pins for the cathode, anode and guard ring.

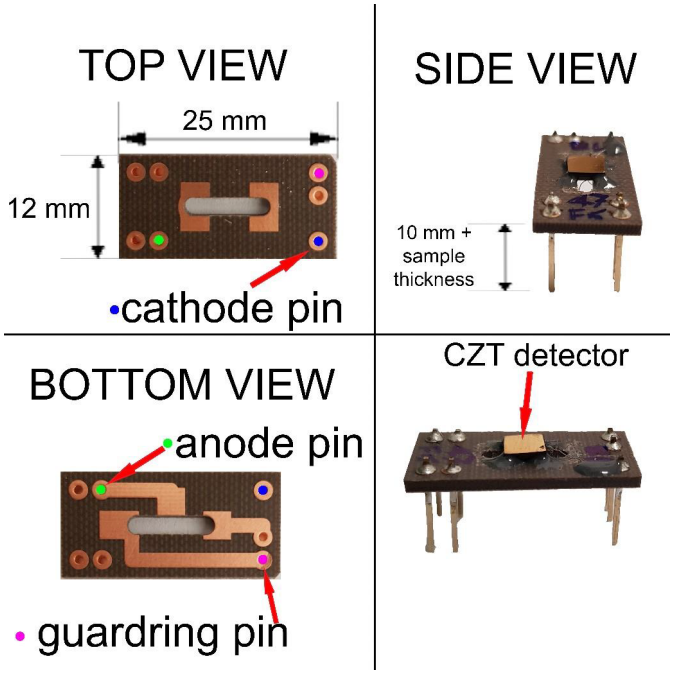

Figure 3.1: The PCB board layout with the important pins, which is used for Sample A and Sample B (taken from [17]).

The electrode contacts on both, Sample A and Sample B, are made out of gold and the cathode covers the whole area on one side of the detector. The anode consists of one pixel with an area size of $2x2^2$. A guard ring (for details see subsection 2.4.1) surrounds the anode [17]. The configuration of Sample A and Sample B with a guard ring is presented in figure 3.2 (a), which also shows an incoming photon that produces electron-hole pairs by interacting with the material. When a bias voltage is applied, the electrons will move to the positive anode and the holes will travel to the cathode. Due to the introduced guard ring, the electronic noise can be reduced [11] and the weighting potential is compressed towards the anode [5]. The shape of a typical signal can be seen in figure 3.2 (b).

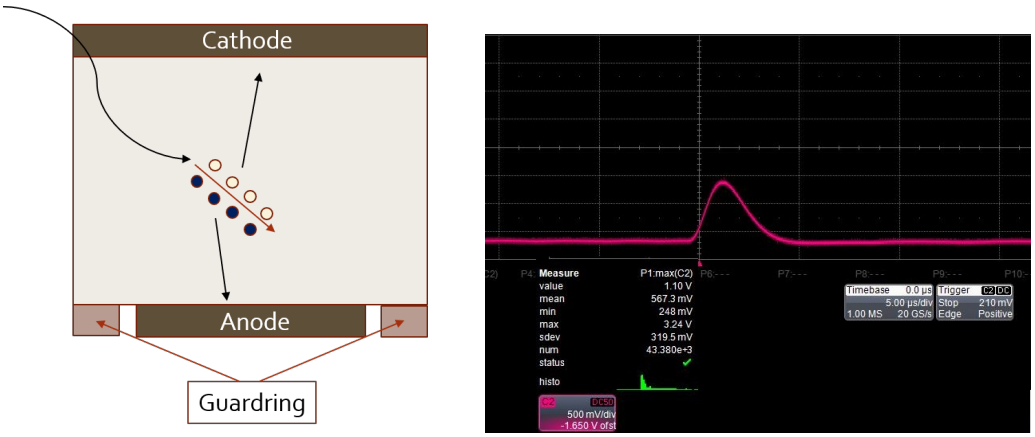

(a) Configuration of a CdZnTe with guard ring.

(b) Exemplary signal of Sample B.

Figure 3.2: (a) The configuration of a CdZnTe with guard ring and (b) an exemplary signal of Sample B. Filled circles represent electrons and open circles holes.

3.1.1 Sample A

Sample A is a CdZnTe sample realized with material from Redlen Technologies. It has a smaller area but is thicker than Sample B with dimensions of 4x4x3 mm^3. As stated above, the anode consists of an area of 2x2 mm^2 [18], leaving the rest of the surface for the guard ring. Figure 3.3 (a) shows Sample A on the PCB board from above, which reveals the cathode that covers the full area. The connection to the anode is indicated by the red wire, the black wire is connected to the cathode and the blue wire to the guard ring. Part (b) of the figure gives an impression of the layout of the anode and guard ring, which are located on the opposite side of the cathode. It also becomes clear that Sample A is rather thick.

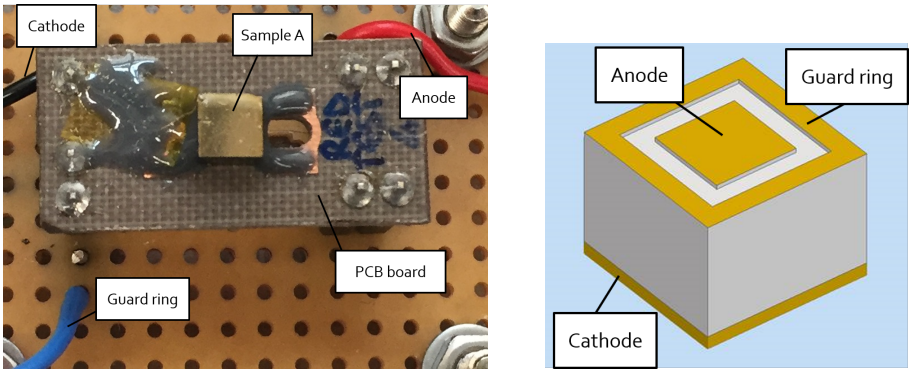

(a) Sample A on the PCB board showing the full-area cathode.

(b) Anode and guard ring layout of Sample A (adapted from a drawing by Doris Pristauz-Telsnigg [19]).

Figure 3.3: Sample A with dimensions of 4x4x3 mm^3 (small & thick) [18].

3.1.2 Sample B

Sample B is made up of standard material produced by the Istituto dei Materiali per l'Elettronica ed il Magnetismo (IMEM) and has a larger area but is thinner than Sample A. The dimensions are 7x5x1 mm^3. Here, the guard ring is larger, as the anode area is still covering only 2x2 mm^2 [18]. A picture of Sample B is provided in figure 3.4 (a). The cathode covers the full area of the CdZnTe and the wires are connected to the anode, cathode and guard ring in the same way as for Sample A. In (b) of figure 3.4 one can see the configuration of the anode and guard ring, revealing that the guard ring covers a larger area than for Sample A, while the CdZnTe is thin.

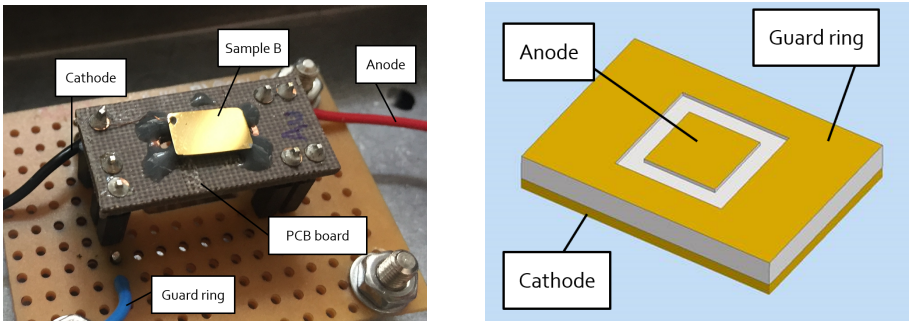

(a) Sample B on the PCB board showing the full-area cathode.

(b) Anode and guard ring layout of Sample B (adapted from a drawing by Doris Pristauz-Telsnigg [19]).

Figure 3.4: Sample B with dimensions of 7x5x1 mm^3 (large & thin)[18].

3.2 CZT/500

Produced by the company RITEC (Latvia) [20], the nuclear radiation detector CZT/500 is based on Cadmium Zinc Telluride (CZT) and intended for γ-spectroscopy for energies above 60 keV. The name derives from the sensitive volume of the detector which is 500 mm^3. The detector has a diameter of 23 mm and a length of 33 mm [16], as can be seen in figure 3.5 (a). Part (b) shows an exemplary shape of a signal of the detector.

(a) The CZT/500 detector produced by RITEC (taken from [16], p.3).

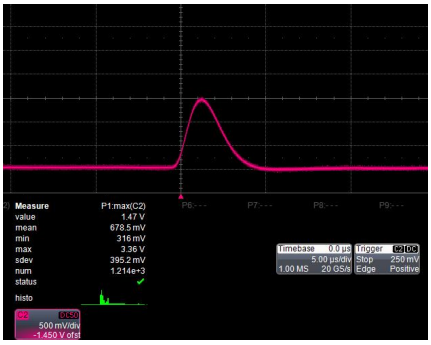

(b) Exemplary signal of the CZT/500 detector.

Figure 3.5: (a) shows the CZT/500 detector and (b) an exemplary signal.

The CZT/500 has a quasi-hemispherical geometry and is biased with a positive high voltage [16]. The geometry is based on the hemispherical geometry introduced in chapter 2.4. Due to manufacturing reasons, the CZT/500 was produced as a quasi-hemispherical geometry which worsens the spectroscopy a little [16]. The cross-sectional view of a quasi-hemispherical detector is shown in figure 3.6 (b). It can be seen that electrons are travelling towards the anode on the top, while holes are moving towards the negative electrode on the sides [20]. In 3.6 (a), the configuration of the semi-cubic CZT/500 can be seen. The positive anode is in the center of the flat surface, the negative electrode is on the spherical outside [20]. The resolution of the CZT/500 is limited by the hole trapping occurring due to impurities in the crystal [16].

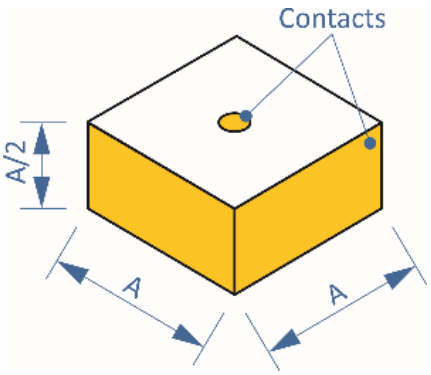

(a) Configuration of the CZT/500 (taken from [16], p.7).

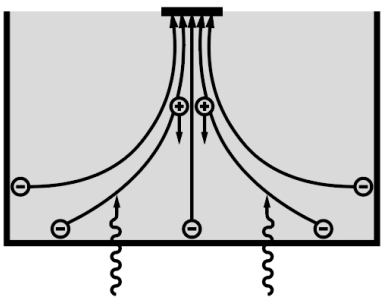

(b) Cross-sectional view of a quasi-hemispherical detector with the anode on the top and the negative electrode on the sides (drawn by Doris Pristauz-Telsnigg [19]).

Figure 3.6: Quasi-hemispherical configuration of the CZT/500.

4 Development of the set up

Despite the fact that the detectors are in principle operable at room temperature, they are still very prone to picking up noise. Therefore, the set up needs to aim towards reducing any noise sources that might interfere. This includes the filtering of the high voltage bias and the shielding of the detector. In addition, the signal needs to be pre-amplified and then amplified. The pre-amplifier and amplifier need to pick up as little noise as possible. Furthermore, the connections between the detector and amplification stages need to be shielded as well, in order to further reduce the noise. The set up was improved stepwise over time, the final version and the involved considerations are stated below.

4.1 HV-Filter

The High Voltage (HV) filter is aiming towards filtering out any fluctuations in the biasing voltages that would introduce noise to the signal. In the final set up, the HV-filter is placed inside a small metallic box, as this enables one to keep the connections between the parts of the filter short, while already shielding it from outside noise. The bias voltages (both for the cathode and the guard ring) are filtered before they enter another metallic box in which the detector is located. The filtering is done in the same way for both, the HV and the guard ring, namely each time through two resistors and a capacitor. The values of the resistors and the capacitor are adapted and improved between the measurements introduced in this thesis. The exact values will be stated before each subsection. All of the parts in the circuit need to sustain high voltage (at least 1000 V) and are chosen accordingly. Figure 4.1 (a) shows the constructed HV-filter and figure 4.1 (b) reflects the underlying circuit diagram. As can be seen in figure 4.1 (a) the circuit is not soldered onto a board but lifted up from the ground. This was done in order to avoid any noise pick-up at unclean soldering nodes or connections on the board [21]. For the experiments, the box is closed with a metallic lid.

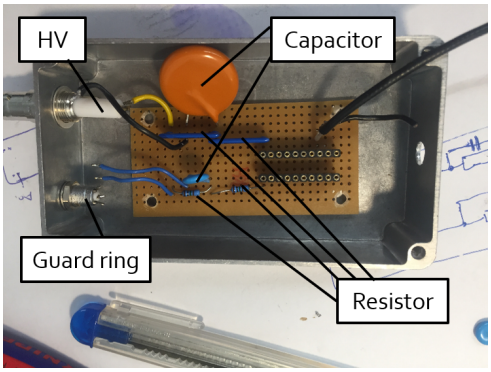

(a) HV-filter in an extra box for biasing voltage of the cathode and guard ring.

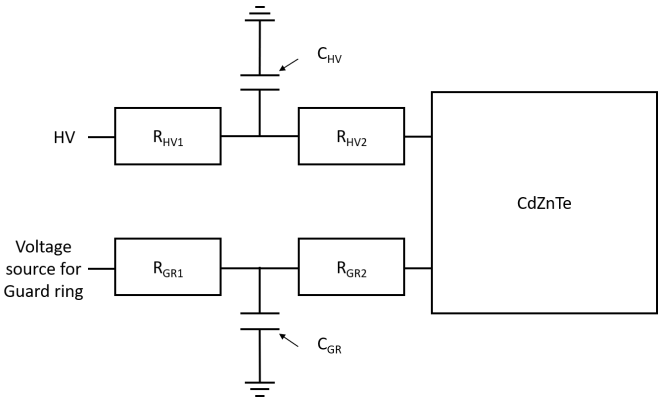

(b) HV-filter circuit diagram.

Figure 4.1: (a) shows the HV-filter and (b) its circuit diagram.

The low-pass filter (consisting of a resistor and a subsequent capacitor that is connected to ground) is responsible for stopping higher frequencies from passing, while letting lower frequencies through. The capacitor C_{HV}/C_{GR} is chosen so that it has a high resistance for alternating currents of low frequencies, while the resistor R_{HV1}/R_{GR1} is chosen small in comparison, which is why the voltage is able to pass the first resistor and to continue along over the second one without any changes [22]. The second resistor R_{HV2}/R_{GR2} helps to stabilize the output. For high frequencies the capacitor C_{HV}/C_{GR} has a small resistance concerning alternating currents and the voltage drop along the first resistor R_{HV1}/R_{GR1} is large [22], resulting in an output voltage of almost zero. This explains why the constructed circuit filters out high frequencies and is able to reduce noise introduced through the high voltage powering the detector.

4.2 Shielding and amplifiers

In order to reduce noise further, the front-end electronics (detector and pre-amplifier) need to be electrically shielded [21]. For the final set up for the measurements with the detectors Sample A and Sample B, two boxes are used. One box contains the HV-filter described in section 4.1. In the other box a board with soldering connections is placed, which has a structure soldered onto it into which the detector Sample A or Sample B can be placed interchangeably. This can be seen in figure 4.2 (a). Only the necessary connections on the board are kept and the soldering nodes are kept as clean as possible, aiming towards reducing the possibility of noise getting picked up there [21].

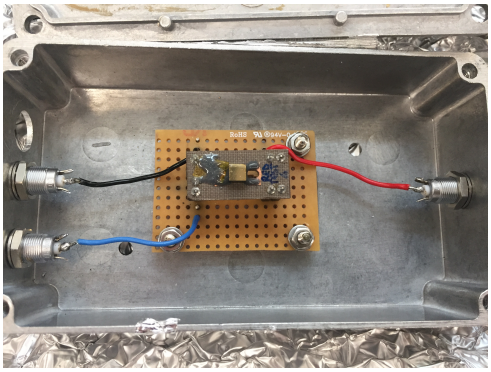

(a) Board with structure for holding Sample A or Sample B.

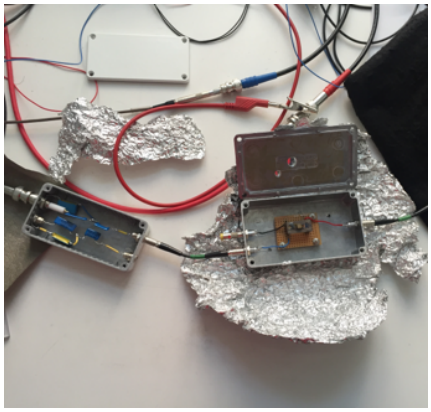

(b) The two boxes containing the HV-filter and the board with the detector.

Figure 4.2: (a) shows the box containing the detector and (b) the set up of the boxes.

The set up with the two boxes is shown in figure 4.2 (b). The boxes can be closed with metallic lids for the experiments and help to reduce outside noise. As can be seen in the set up (see figure 4.2 (b)), the connection cables between the boxes are chosen as short as possible to avoid any unnecessary capacitance [21]. In order to shield the HV-filter and the detector from outside noise sources as much as possible, the metallic boxes and cables are additionally wrapped with aluminium foil. The aluminium foils can also be seen in figure 4.2 (b). The signals improve greatly with the introduction of the aluminium layers around the boxes and connection cables. Furthermore, a black cloth is placed over the box containing Sample A or Sample B, to minimize light sources that can create unwanted signals.
Another aspect to consider is that no ground loops should be present in the set up, which can introduce an undesired 50 Hz signal. A current, for example created through a radio frequency signal close by, could enter in one ground point and exit at another. This would result in a current passing the detector and/or pre-amplifier ground connection [21]. Therefore, it is ensured that there is only one ground point present. In addition, the pre-amplifier is not placed directly next to the amplifier, but at a little distance to avoid any feedback between them [21].

The detector signals need to be pre-amplified and amplified. Two different pre-amplifiers are used in this thesis, depending on the measurement. These are the charge-sensitive AMPTEK 250 on the PC250 Test Board [23] (see figure 4.3 (a)) and the charge-sensitive, low-noise RITEC pre-amplifier PA101C No.804 [24] (see figure 4.3 (b)). The AMPTEK 250 pre-amplifier can be used with different detectors, such as CdZnTe, CdTe or photomultiplier tubes. It is operated with $\pm$ 6 V, can accept positive and negative input signals and yields an inverse polarity of the output signal [23]. The RITEC pre-amplifier PA101C No.804 is specifically designed to be used for γ-spectroscopy with semi-conductor detectors at room temperature. It can also accept both,

positive and negative input, is operated with ± 12 V and yields an inverted output signal relative to the input signal [24]. Both pre-amplifiers are powered by the GwINSTEK GPD-4303S DC Power Supply. The AMPTEK 250 is placed into a metallic box, which greatly helps to reduce external noise, while the RITEC pre-amplifier PA101C No.804 already comes with its own shielding structure.
In addition, the pre-amplifiers and the connections from the box containing the detector to the pre-amplifier are shielded with layers of aluminium foil, as this improves the signal further. Both pre-amplifiers are tested and used with Sample A and Sample B, as the focus of this thesis is to establish first basic electronics for these detectors. For the CZT/500 detector only the RITEC pre-amplifier PA101C No.804 is used, as it is specifically manufactured to be used together with this detector and measurements with it are mainly aimed towards comparison with the other two samples.

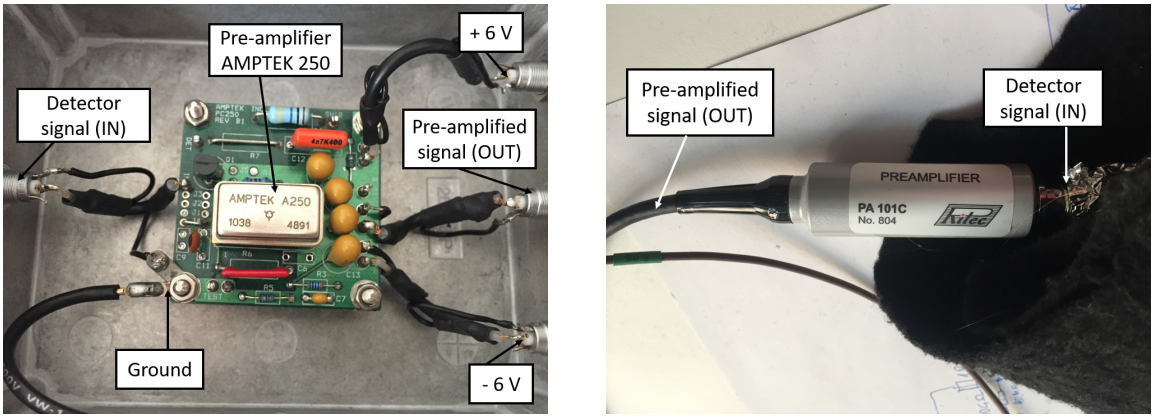

(a) PC250 Test Board with the pre-amplifier AMPTEK 250.

(b) RITEC pre-amplifier PA101C No.804.

Figure 4.3: Pre-amplifiers used.

Further, in all the measurements included in this thesis the CAEN Mod. N5688 16CH Spectroscopy Amplifier (see figure 4.4) is used as an amplifier after the pre-amplification stage. The controller that can be seen in figure 4.4 allows to change settings, such as the gain value and the shaping time. The values are stated for each measurement. The amplifier is placed in a crate and can accept positive and negative signals [25].

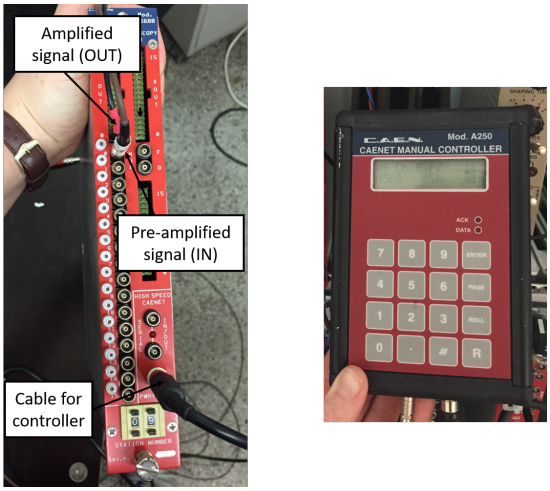

Figure 4.4: CAEN Mod. N5688 16CH Spectroscopy Amplifier and controller module.

5 Characterization

Aim of this thesis is to perform first characterizations of the detectors Sample A and Sample B. Therefore, the following sections introduce different configurations (e.g. various HV values, biasing the anode or cathode) that are tested with Sample A and Sample B, in order to obtain the best possible signal outputs. In addition, some measurements are also performed with the CZT/500 detector as a reference point for comparison and to check feasibility.
For all measurements the Tennelec TC 953 high voltage module and a LeCroy SDA 760Zi-A 6GHz oscilloscope are used, as well as the mentioned CAEN Mod. N5688 16CH Spectroscopy Amplifier (see section 4.2). In all the following analyses, errors of the measurement values are calculated by assuming a Poisson distribution of the number of radioactive decays within any given time interval, resulting in the square root of the measured value as its estimated standard error. The peaks of interest are fitted with the program QtiPlot. More specifically, the width of the peak (i.e. the standard deviation) is determined by fitting a (double) Gaussian distribution. As an underlying normal distribution is assumed, one can calculate the Full Width at Half Maximum (FWHM) with the width value σ, following this formula [26]:

$$FWHM = 2.35 \cdot \sigma. \tag{5.1}$$

It is desirable to have a low FWHM, which indicates a high resolution. The plots of the spectra are done with QtiPlot [27]. They show the measured amplitude in Volt on the x-axis and the counts per Volt-binning (the size of which is indicated) on the y-axis if not stated differently. All other plots are created with R [28] in RStudio [29].

5.1 Current-voltage characterization

First, a current-voltage characterization is performed for Sample A and Sample B. The Tennelec TC 953 high voltage module, which has a resolution of ± 1V, is used to produce the needed bias voltage. As one is only interested in obtaining the current-voltage relationship, no filtering of the high voltage is performed. Biasing the cathode with a negative bias voltage at room temperature yields a leakage current, which is the current that is present due to conductive paths even without direct irradiation. Therefore, this current can give insights into possible problems in the detector, as it will change when defects or damages are present in the detector [30]. The Tennelec TC 953 also reports on this leakage current.
Figure 5.1 shows the current-voltage characteristics for Sample A in the voltage range -500 to -1000 V. The current is reported for 100 V steps in four different measurements. The overall linear fit has an R^2 of 0.95, which confirms the visual impression that there is a high linear association between current and voltage in this voltage range. For Sample B the changes in the current for voltages between -500 V and -900 V are too small to get registered by the Tennelec

TC 953, which has a resolution of ± 10 nA. In this range, the leakage current for Sample B is constant with 10 nA. Only at -1000 V does the current go up to 20 nA.
These results show that the leakage current for Sample A at -1000 V bias voltage is 140 nA. Due to the fact that Sample B is thinner, biasing the cathode with a negative bias voltage of -1000 V at room temperature yields a smaller leakage current of 20 nA.

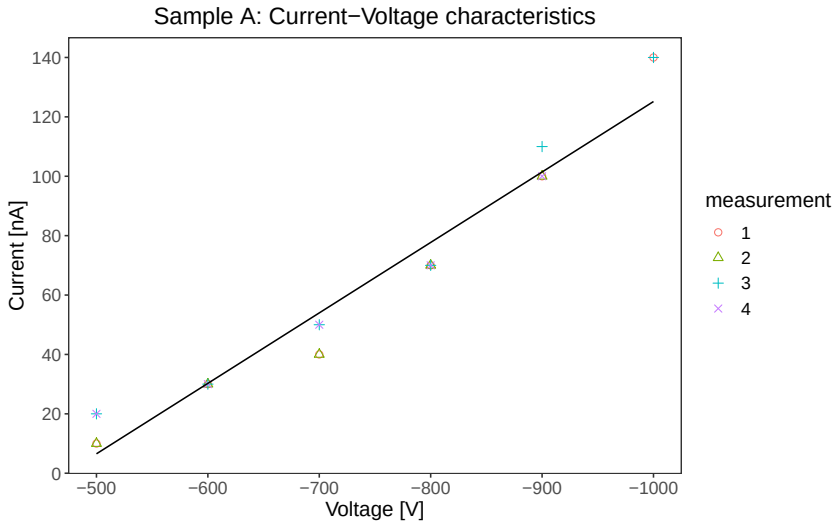

Figure 5.1: Current-Voltage characteristics of Sample A for four measurements and an overall linear fit (R^2 = 0.95). The current is reported every 100 V between -500 and -1000 V.

5.2 Measurements with the AMPTEK 250

First successful measurements with the amplifier CAEN Mod. N5688 16CH Spectroscopy Amplifier are performed with the AMPTEK 250 pre-amplifier (see in section 4.2 figure 4.3 (a) for a picture). The shielding of the pre-amplifier, described in section 4.2, reduces the noise greatly. However, as Sample B is thinner than Sample A and therefore more susceptible to noise, the following measurements are only performed with Sample A, as the signal for Sample B is too noisy for any interpretable results.

5.2.1 Various bias voltage values

First, for this measurement the guard ring is not biased but rather connected to ground. The HV-filter has the same structure as described in section 4.1 and figure 4.1. The values of both resistors R_{HV1} and R_{HV2} are 100 MΩ and the capacitor C_{HV} has a capacitance of 10 nF. Na-22 (β^+-decay [31]) is used as an irradiation source and placed directly on top of the box in which Sample A is connected. The amplifier settings are a gain of 7 and a shaping time of 0.2 μs.

Measurements with -500 V, -600 V and -800 V are performed. The results of the FWHM

are reported in table 5.1 and figure 5.2. When comparing the spectra themselves (see figure 5.3 (a)-(c)) it becomes evident that the higher bias voltages of -600 V and -800 V show a more intense 511 keV annihilation peak (at around 0.1 V) than the bias voltage -500 V, because of better charge collection. The larger values in the y-axis for -500 V stems from a longer data taking period. In addition, the 1275 keV (at around 0.25 V) is not visible in the -500 V measurement and starts to slightly appear for the two higher bias voltages. This is expected and reflects the, in general, better charge collection at higher bias voltages as the charges are accelerated faster towards the electrodes, resulting in less charge loss and trapping on the way. However, when comparing the FWHM values, their standard deviations (extracted from the fit) and their 95% confidence intervals, one can see that these get larger with higher bias voltage. The FWHM and their std values are getting larger as can be seen in table 5.1, maybe due to the use of a quite simple fit function.
Now, the goal is to reduce the noise and increase the charge collection further.

	-500 V	**-600 V**	**-800 V**
FWHM ± std	(10.3 ± 0.7) mV	(11 ± 1) mV	(12 ± 2) mV

Table 5.1: FWHM values of the 511 keV annihilation peak of Na-22 in mV for -500 V, -600 V and -800 V bias voltage for Sample A with the pre-amplifier AMPTEK 250 and the corresponding standard deviations.

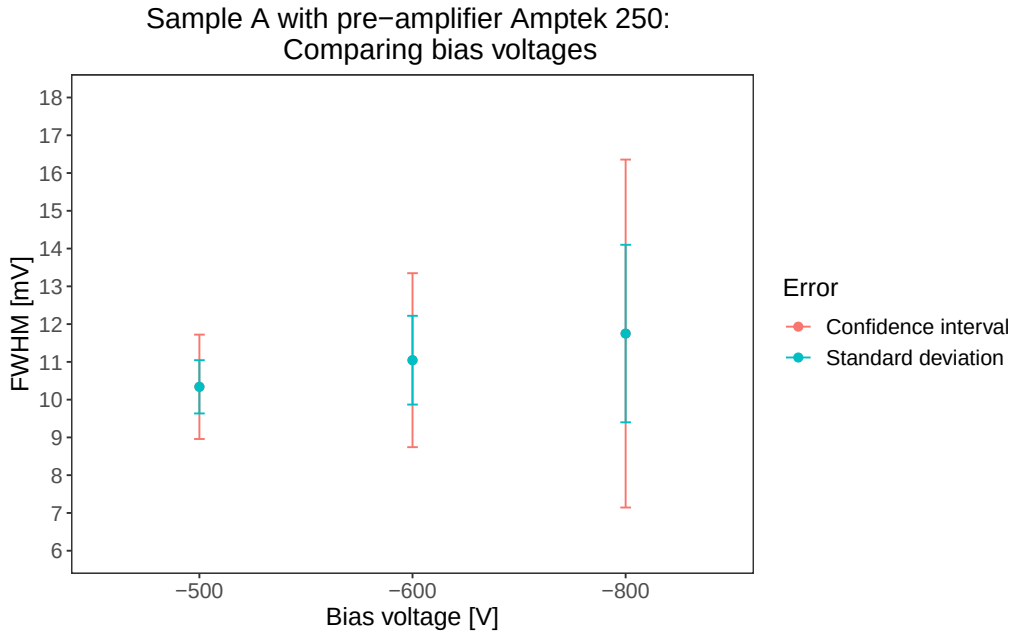

Figure 5.2: Different bias voltages for Sample A with the pre-amplifier AMPTEK 250 and the corresponding FWHM values of the 511 keV annihilation peak of Na-22. Orange error bars indicate the 95% confidence interval, turquoise error bars represent the standard deviation of the values for -500 V, -600 V and -800 V.

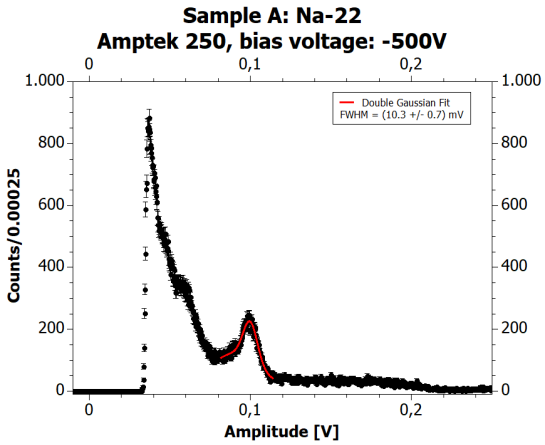

(a) Bias voltage of -500 V.

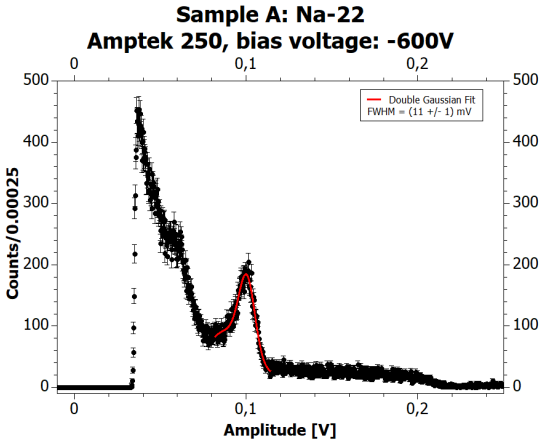

(b) Bias voltage of -600 V.

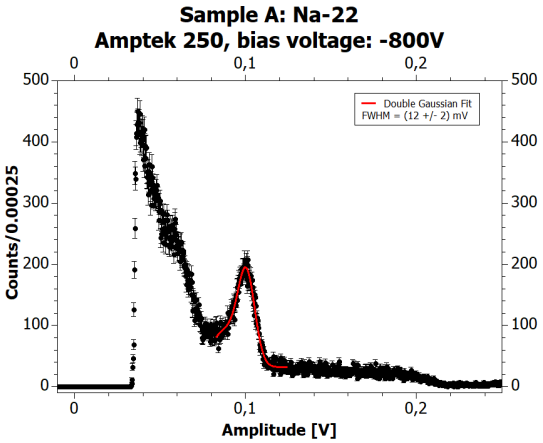

(c) Bias voltage of -800 V.

Figure 5.3: Plots of bias voltage measurements with Sample A and the pre-amplifier AMPTEK 250 at (a) -500 V, (b) -600 V and (c) -800 V with Na-22 as irradiation source.

5.2.2 Including the guard ring

When one connects and biases the guard ring as well, a greater potential difference between guard ring and anode is created. The field lines of the electrical field in the detector are concentrated even more towards the anode. Due to this, the charge collection and noise level should improve, when the guard ring is biased too [30]. Therefore, the same set up as for the measurements of subsection 5.2.1 is used with the only change that now the guard ring is biased as well. The filter for the bias voltage for the guard ring consists of two resistors R_{GR1} and R_{GR2} of 1 MΩ value and one capacitor C_{GR} between them of 10 nF.

Two bias voltages are tested in more detail: -500 V and -600 V. For both of them, measurements are done with the guard ring being biased from -20 V to -100 V in 20 V steps. The

results for the measurements of -20 V and -100 V are reported here as an example. Figure 5.4 illustrates the results of the measurements. It quickly becomes evident that biasing the guard ring does not yield the expected improvement, when inspecting the plots visually. The results of the calculated FWHM, reported in table 5.2, show that they worsen greatly when including the guard ring, which is unexpected at first. However, it must be noted that, in order to bias the guard ring as well, an additional bias voltage filter circuit needs to be included. Therefore, an additional noise source is introduced that can disturb the signal. This is what can be seen in the plots of figure 5.4, as the 511 keV peak is not well separated from the noise peak at the beginning of the spectra. Therefore, an improvement of the set up is necessary.

	-500 V	**-600 V**
-20 V	(21 ± 12) mV	(24 ± 7) mV
-100 V	(19 ± 9) mV	(24 ± 9) mV

Table 5.2: FWHM values and the corresponding standard deviations of the 511 keV annihilation peak of Na-22 in mV for -500 V and -600 V bias voltage and a biasing voltage of -20 V and -100 V for the guard ring for Sample A with the pre-amplifier AMPTEK 250.

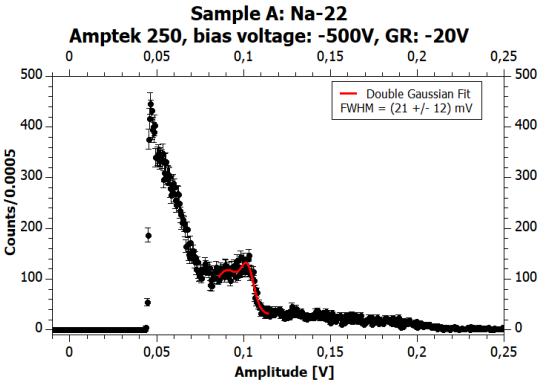

(a) Bias voltage of -500 V and a guard ring bias voltage of -20 V.

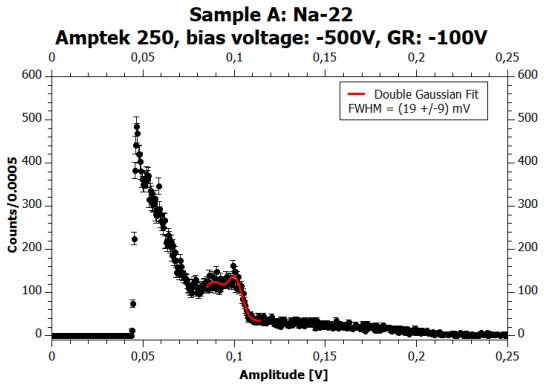

(b) Bias voltage of -500 V and a guard ring bias voltage of -100 V.

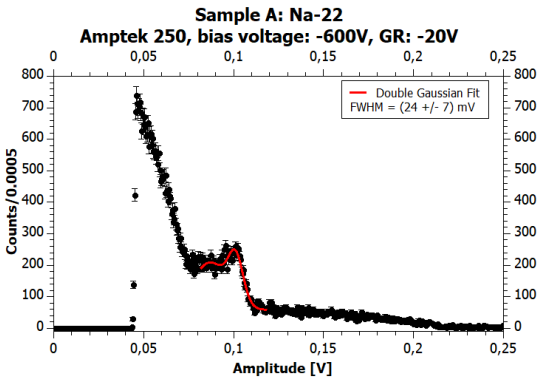

(c) Bias voltage of -600 V and a guard ring bias voltage of -20 V.

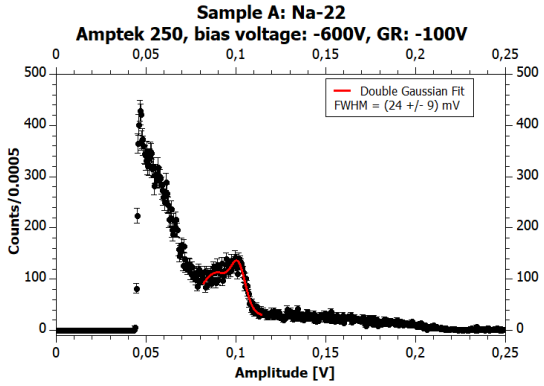

(d) Bias voltage of -600 V and a guard ring bias voltage of -100 V.

Figure 5.4: Plots of bias voltage measurements with Sample A and the pre-amplifier AMPTEK 250 at -500 V and -600 V with bias voltages of -20 V and -100 V for the guard ring with Na-22 as irradiation source.

Comparing the differences in results between a bias voltage of -20 V and -100 V for the guard ring for the measurement with a bias voltage of -500 V, it appears as if a higher bias voltage of the guard ring does yield better results, when comparing the FWHM results. However, for the -600 V measurement this pattern is not so obvious and the benefits of including a guard ring need to be investigated further with an improved set up that is less susceptible to noise.

5.3 Biasing the cathode with the RITEC pre-amplifier

Noise sources are the pre-amplifier, amplifier, connection cables, the detector itself and the filter. Short connection cables and different strategies of shielding (e.g. aluminium foil, boxes, lifting the elements of the filter up, etc. - see for details section 4.2) are already implemented as much as possible. Therefore, the only parts that still can be improved are the amplifiers. Measurements with different amplifiers have shown that the CAEN Mod. N5688 16CH Spec-

troscopy Amplifier yields the best results in terms of the least noise. Despite the shielding, the AMPTEK 250 pre-amplifier is still rather susceptible to noise (e.g. the box it is placed in is not sealed but can be opened when needed) and the pre-amplifier also has a large area which increases the chances of picking up noise.
Due to these reasons, the RITEC pre-amplifier PA101C No.804 is used for measurements with Sample A and Sample B. It is already manufactured in such a way that noise pick-up is greatly reduced. Therefore, one expects that the measurement results will improve greatly and that also measurements with biasing the guard ring will show improved results.
The settings of the amplifier are adjusted towards the RITEC pre-amplifier. The shaping time is set to 3 μs and the gain to 4.

The RITEC pre-amplifier provides an internal HV-filter that can be used for the CZT/500 detector, which is biased at the anode. The bias voltage first passes this internal HV-filter before it reaches the detector whose output signal then passes the pre-amplifier stage. Here, we are interested in the performance of Sample A and Sample B, when biased from the cathode. Therefore, the HV-filter for Sample A and Sample B is constructed in almost the same way as within the RITEC pre-amplifier structure. This yields a circuit connected to the cathode and high voltage module with one resistor R_{HV1} of 100 MΩ and one (R_{HV2}) of 200 MΩ value. In between there is a capacitor C_{HV} of 220 nF.

5.3.1 Excluding the guard ring

For a first test of the new set up, the guard ring is grounded in the following measurement. A Co-57 source (electron capture [31]) is used for irradiation. The typical γ-peaks are at 122 keV and 136.5 keV [31]. One benchmark for the energy resolution is already to be able to distinguish these two peaks from one another.
Figure 5.5 shows a measurement of Sample A with a bias voltage of -800 V. The overall noise level is acceptable and one can clearly distinguish the two peaks (the higher peak corresponds to 122 keV, the smaller one to 136.5 keV) . However, the 122 keV peak is very broad with a FWHM of (37 ± 21) mV, suggesting that the charge is not collected very well. Biasing the guard ring might increase the charge collection.

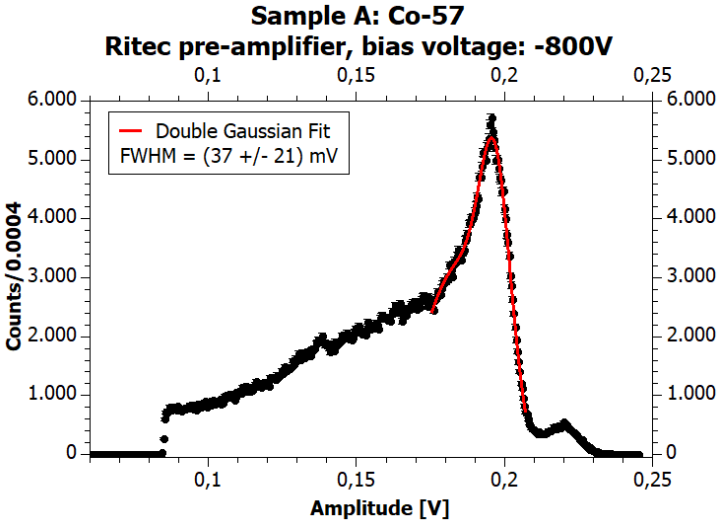

Figure 5.5: Spectrum of a Co-57 source with Sample A and the RITEC pre-amplifier. The bias voltage is -800 V.

5.3.2 Including the guard ring

The guard ring is included to increase the charge collection. For this, a filter for the bias voltage for the guard ring is constructed. It has the same values and structure as the filter for the bias voltage (i.e. R_{GR1} = 100 MΩ, R_{GR2} = 200 MΩ and C_{GR} = 220 nF). The circuit is represented in figure 5.6. The settings for the amplifier are a shaping time of 1 μs and a gain of 5. The measurements are performed with a Co-57 (electron capture [31]) source.

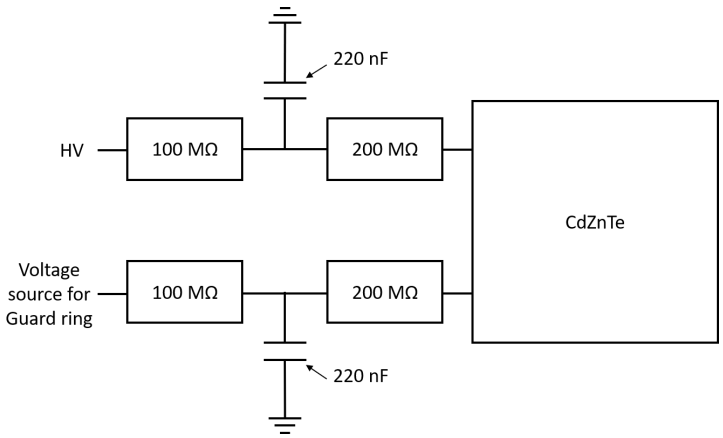

Figure 5.6: HV-filter circuit for measurements with the RITEC pre-amplifier.

5.3.2.1 Sample A

Measurements in 50 V steps are performed with Sample A between bias voltages of -700 V and -1000 V with guard ring values between -7 V and -13 V with a Co-57 source. Two of the seven spectra are shown as examples in figure 5.7, namely the measurements with - 750 V and a guard

ring of -8 V and -950 V and -12 V. Table 5.3 gives the corresponding FWHM and their std values. A comparison between the measurements is reported through figure 5.8, in which the turquoise error bars indicate the Standard deviation (std) of the fit for the 122 keV peak of Co-57 and the orange error bars the 95% confidence interval. The error bars are overlapping, but the lowest result is achieved with -800 V bias voltage and a guard ring of -9 V. It is therefore decided to investigate the influence of the guard ring on the FWHM further with a bias voltage of -800 V.

	bias: -750 V, GR: -8 V	**bias: -950 V, GR: -12 V**
FWHM ± std	(22 ± 1) mV	(24 ± 5) mV

Table 5.3: FWHM values and the corresponding standard deviations of the 122 keV annihilation peak of Co-57 in mV for -750 V bias voltage and -8 V guard ring voltage and -950 V bias voltage and -12 V guard ring voltage for Sample A with the RITEC pre-amplifier.

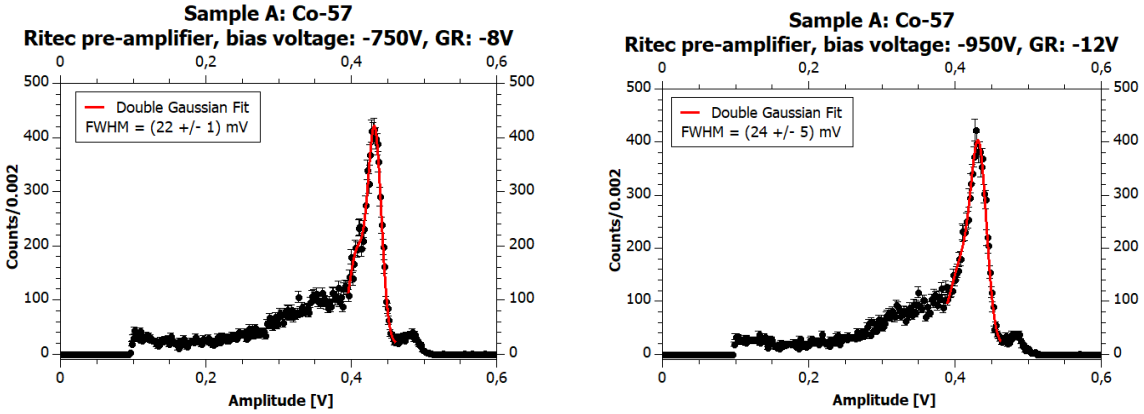

(a) Bias voltage of -750 V and a guard ring bias voltage of -8 V.

(b) Bias voltage of -950 V and a guard ring bias voltage of -12 V.

Figure 5.7: Plots of different bias voltage measurements with Sample A and the RITEC pre-amplifier at (a) -750 V bias voltage and -8 V guard ring (GR) voltage, as well as a bias voltages of (b) -950 V and -12 V guard ring voltage.

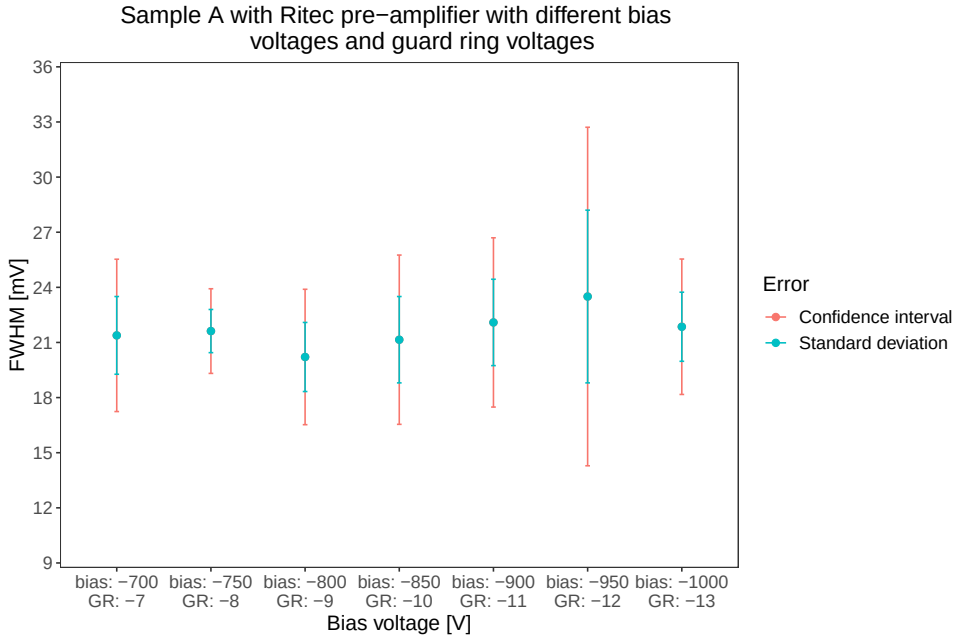

Figure 5.8: Different guard ring (GR) bias voltages for Sample A with the RITEC pre-amplifier at different bias voltages and the corresponding FWHM values of the 122 keV annihilation peak of Co-57. Orange error bars indicate the 95% confidence interval, turquoise error bars represent the standard deviation of the values.

For deeper inspection, a bias voltage of -800 V is used for Sample A and the guard ring is biased with values between -8 V and -22 V in one volt steps. Figure 5.9 shows two plots of the measurement series and table 5.4 gives the corresponding FWHM values. When comparing the spectra without biasing the guard ring (see figure 5.5) with the ones including it (see figure 5.9), one can directly see the improvement achieved through the inclusion of the guard ring. The fitted peak is a lot sharper and thinner, which is also reflected by the FWHM reported. In addition, visual inspection shows that also the 136.5 keV peak is sharper and clearly distinguishable from the 122 keV peak.

	-8 V	**-15 V**
FWHM ± std	(19 ± 2) mV	(22 ± 2) mV

Table 5.4: FWHM values of the 122 keV peak of Co-57 in mV for -800 V bias voltage and -8 V and -15 V guard ring bias voltage for Sample A with the RITEC pre-amplifier and the corresponding standard deviations.

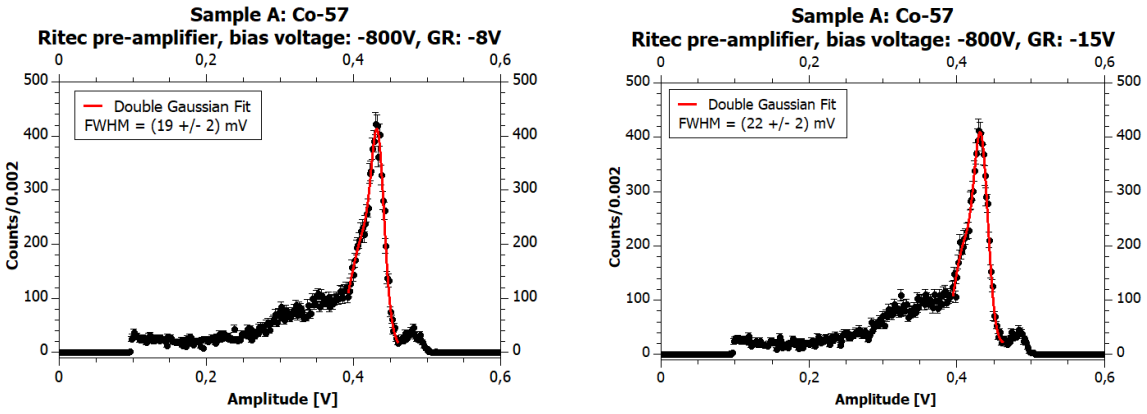

(a) Bias voltage of -800 V and a guard ring bias voltage of -8 V.

(b) Bias voltage of -800 V and a guard ring bias voltage of -15 V.

Figure 5.9: Plots of measurements with Sample A and the RITEC pre-amplifier at -800 V with bias voltages of (a) -8 V and (b) -15 V for the guard ring (GR) with Co-57 as irradiation source.

The values for all measurements with Sample A and the RITEC pre-amplifier, when also biasing the guard ring, are reported in figure 5.10. The bias voltage is -800 V and the FWHM values for each value of bias voltage for the guard ring between -8 V and -22 V are reported. The turquoise error bars indicate the Standard deviation (std) of the fit for the 122 keV peak of Co-57, the orange error bars the 95% confidence interval. The measurements for -8 V and -9 V seem to produce lower Full Width at Half Maximum values, while the error bars for -11 V guard ring bias voltage are the smallest ones. On the other hand, when comparing the 136.5 keV peak visually in figure 5.9 a higher bias voltage of the guard ring seems to show a better collection for this peak. However, one can also see from figure 5.10 that all of the measurements yield values that are within each others' confidence intervals, as well as within the standard deviation. Therefore, it is not possible to report on a statistically significant best value. In general, one needs to be careful with the interpretation of the fit results as the simple fit function used is not the correct response function of the detector, since only a general characterization of the detectors is the goal of this thesis.

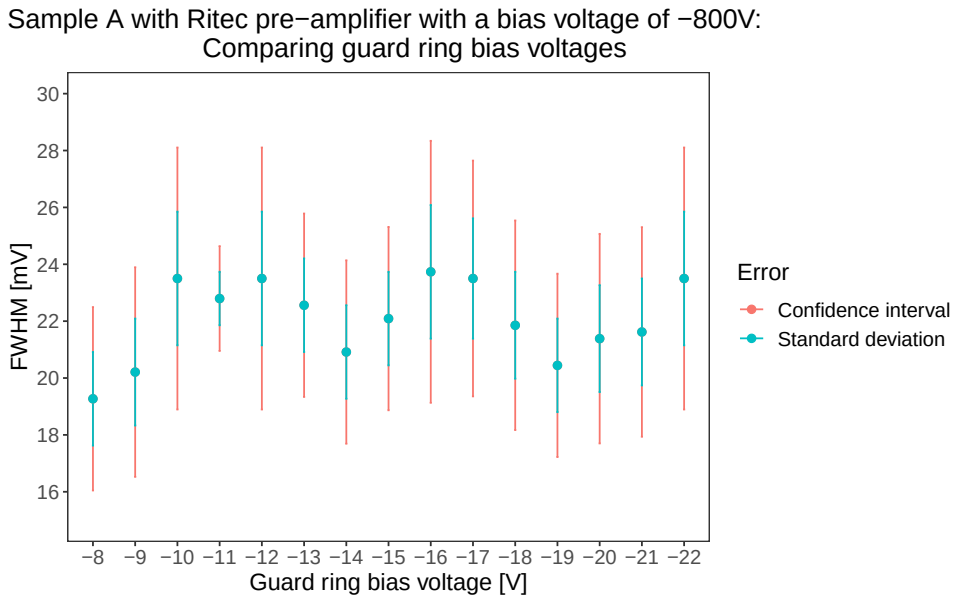

Figure 5.10: Different guard ring bias voltages for Sample A with the RITEC pre-amplifier at -800 V bias voltage and the corresponding FWHM values of the 122 keV annihilation peak of Co-57. Orange error bars indicate the 95% confidence interval, turquoise error bars represent the standard deviation of the values for measurements between -8 V and -22 V in one volt steps.

5.3.2.2 Sample B

As Sample B is a lot thinner and therefore more susceptible to picking up noise, only measurements with the guard ring yield interpretable results. Therefore measurements with different bias voltages and guard rings are performed. In steps of 50 V the bias voltage is changed from -300 V to -650 V. The range is chosen smaller compared to Sample A, due to the reason that Sample B is smaller and should not require such high bias voltage [30]. The guard ring values change in 1 V steps starting from -3 V to -10 V. The set up is the same as for the measurements with Sample A and also here a Co-57 source is used. Figure 5.11 shows two example spectra of the measurement series. The corresponding values are reported in table 5.5. The measurements with -350 V bias voltage and -4 V guard ring voltage and -550 V bias and -8 V guard ring voltage are shown. The FWHM values of all the measurements are reported in figure 5.12 for comparison. The turquoise error bars show the Standard deviation (std) of the fit for the 122 keV peak of Co-57, while the orange error bars show the 95% confidence interval.
The FWHM values are in general a lot higher than for Sample A, which is also noticeable when comparing the spectra in figure 5.11. Sample B shows a less pronounced 122 keV peak (here around 0.4 V) with a lot of noise pick up in lower energy regions. In addition, the 136.5 keV peak (here around 0.45 V) is hard to distinguish, which further reflects the higher susceptibility to noise. When comparing the different bias voltages, it should be noted that the error bars are often overlapping. However, -600 V with a guard ring bias voltage of -9 V yields the lowest Full Width at Half Maximum value. This could show a statistical fluctuation or a true improvement

at -600 V. The bias voltage of -600 V will be further investigated with different bias voltages.

	bias: -350 V, GR: -4 V	**bias: -550 V, GR: -8 V**
FWHM ± std	(33 ± 5) mV	(52 ± 5) mV

Table 5.5: FWHM values and the corresponding standard deviations of the 122 keV annihilation peak of Co-57 in mV for -350 V bias voltage and -4 V guard ring (GR) voltage and -550 V bias voltage and -8 V guard ring voltage for Sample B with the RITEC pre-amplifier.

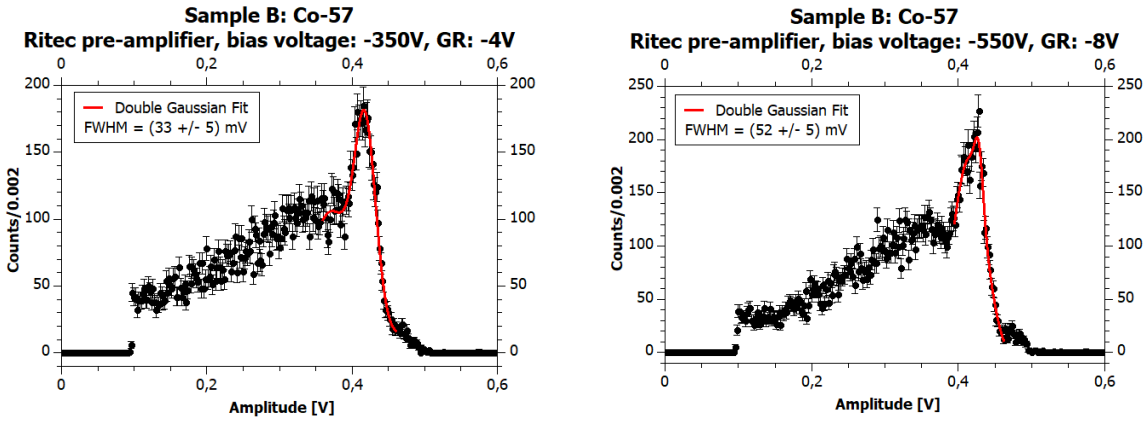

(a) Bias voltage of -350 V and a guard ring bias voltage of -4 V.

(b) Bias voltage of -550 V and a guard ring bias voltage of -8 V.

Figure 5.11: Plots of different bias voltage measurements with Sample B and the RITEC pre-amplifier at (a) -350 V bias voltage and -4 V guard ring (GR) voltage, as well as a bias voltages of (b) -550 V and -8 V guard ring voltage.

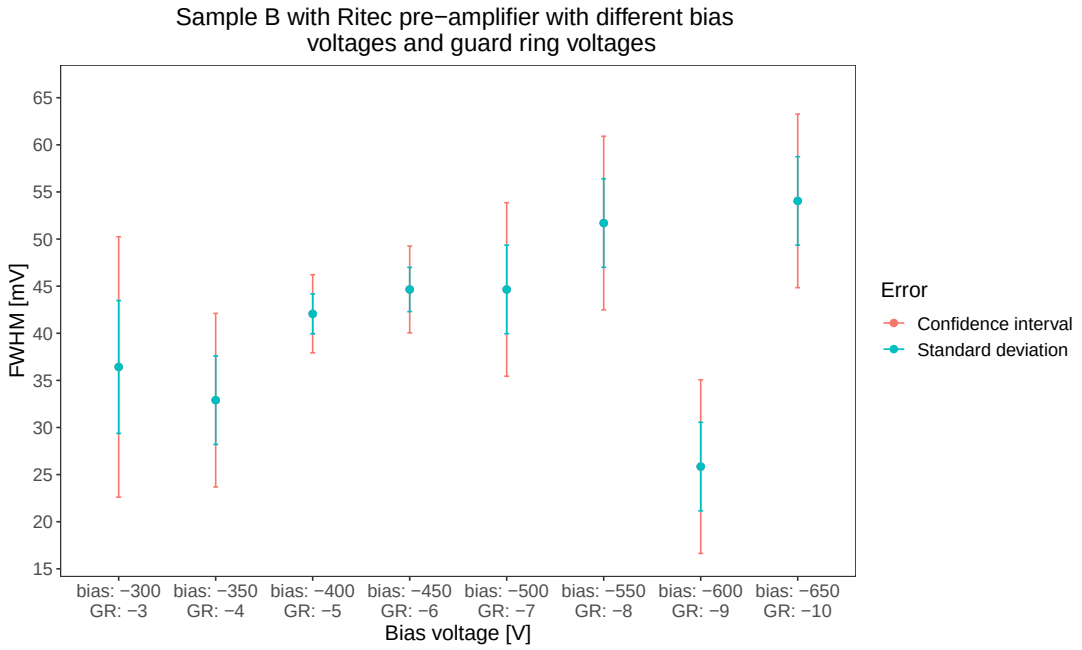

Figure 5.12: Different guard ring bias voltages for Sample B with the RITEC pre-amplifier at different bias voltages and the corresponding FWHM values of the 122 keV annihilation peak of Co-57. Orange error bars indicate the 95% confidence interval, turquoise error bars represent the standard deviation of the values.

Measurements with -600 V as a bias voltage with Sample B are performed. Different bias voltages for the guard ring are tested, ranging from -8 V to -13 V. As impressions, two figures of spectra are shown in figure 5.13. One of them represents the measurement with a guard ring bias voltage of -9 V, the other a guard ring bias voltage of -13 V. The corresponding FWHM and std values can be found in table 5.6. The 136.5 keV peak is more visible for these measurements than the ones with -330 V or -550 V bias voltage from figure 5.12. The charge collection is improved as well, as can be seen when looking at the FWHM values. When comparing plot (a) and (b) in figure 5.13 one can see that the noise level seems reduced for the measurement with a guard ring bias voltage of -13 V. However, it should be noted that more counts are reported in this spectrum, as the collection time is longer. This shows that an extended measuring period does improve the accuracy, which is also reflected in the improved standard deviation of plot (b).

	-9 V	**-13 V**
FWHM ± std	(26 ± 5) mV	(28.0 ± 0.7) mV

Table 5.6: FWHM values of the 122 keV peak of Co-57 in mV for -600 V bias voltage and -9 V and -13 V guard ring bias voltage for Sample B with the RITEC pre-amplifier and the corresponding standard deviations.

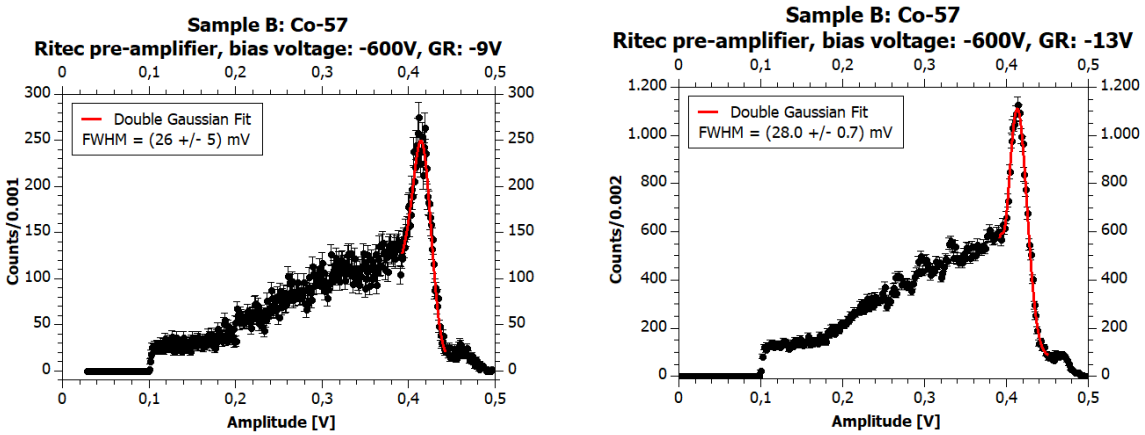

(a) Bias voltage of -600 V and a guard ring bias voltage of -9 V.

(b) Bias voltage of -600 V and a guard ring bias voltage of -13 V.

Figure 5.13: Plots of measurements with Sample B and the RITEC pre-amplifier at -600 V with bias voltages of (a) -9 V and (b) -13 V for the guard ring (GR) with Co-57 as irradiation source.

Figure 5.14 shows an overview of all the FWHM values of the 122 keV peak of Co-57 of the measurement series with Sample B and a bias voltage of -600 V. The orange error bars show the 95% confidence interval and the turquoise ones the standard deviation. The FWHM results lie within each others' error bars and show a similar value for all the measurements around 29 mV. Thus suggesting that the outlying value presented in figure 5.12 for a bias voltage of -600 V is not purely random. The only exception is a guard ring bias voltage of -9 V which yields a value of 26 mV. However, when looking at figure 5.14, one can clearly see that the error bars are by far larger for this measurement and the result should therefore be treated with caution.

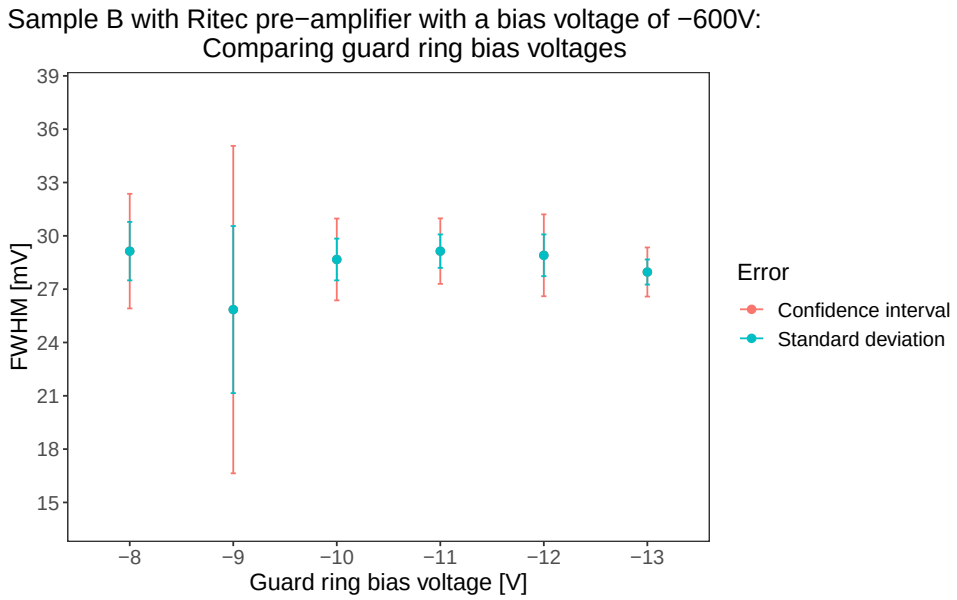

Figure 5.14: Different guard ring (GR) bias voltages for Sample B with the RITEC pre-amplifier at -600 V bias voltage and the corresponding FWHM values of the 122 keV annihilation peak of Co-57. Orange error bars indicate the 95% confidence interval, turquoise error bars represent the standard deviation of the values for measurements between -8 V and -13 V in 1 V steps.

5.4 Biasing the anode with the RITEC pre-amplifier

In order to be able to compare Sample A and Sample B and their performance with the CZT/500 detector, a set up is constructed that works for all of them. For this, the pre-amplification is carried out with the pre-amplifier RITEC pre-amplifier PA101C No.804. In contrast to the measurements up to this point, the anode and not the cathode is biased. Therefore, the bias voltage is positive. This is needed, as the CZT/500 detector can only be positively biased through the anode [16]. Now the internal high voltage filter of the RITEC pre-amplifier can be used for the bias voltage.

5.4.1 Various bias voltage values

First, measurements with different positive bias voltages are performed for all three detectors. As no guard ring is biased, only the internal high voltage filter of the RITEC pre-amplifier is used. The settings for the CAEN amplifier are a gain of 4 and a shaping time of 3 μs for Sample A and Sample B.

5.4.1.1 Sample A

Three different positive bias voltages are tested with Co-57 (electron capture [31]), namely +600 V, +800 V and +1000 V. The spectra can be seen in figure 5.15 and the corresponding FWHM

values in table 5.7. After the measurement of +600 V the trigger level is turned up in order to cut out the noise peak that is pronounced for the measurement with a bias voltage of +600 V. The results in table 5.7 show an improved FWHM when compared to the measurements for which the cathode is biased (see figure 5.5). However, when looking at figure 5.15, one can clearly see that the measurements of +800 V and +1000 V bias voltage show worse performance. Not only is the 136.5 keV peak not visible, but also the general noise level seems to be increasing with higher bias voltage.

	+600 V	**+800 V**	**+1000 V**
FWHM ± std	(17.6 ± 0.9) mV	(17 ± 2) mV	(23 ± 2) mV

Table 5.7: FWHM values of the 122 keV peak of Co-57 in mV for +600 V, +800 V and +1000 V bias voltage for Sample A when biasing the anode and the corresponding standard deviations.

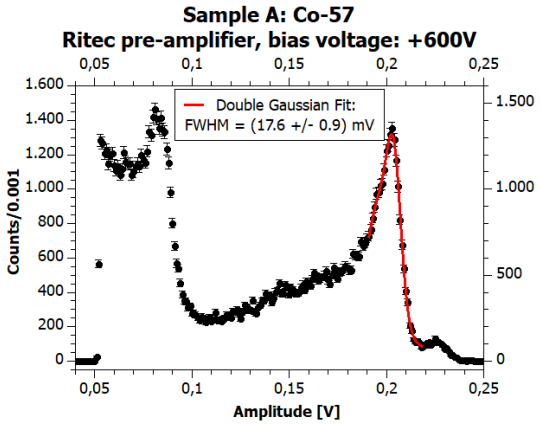

(a) Bias voltage of +600 V.

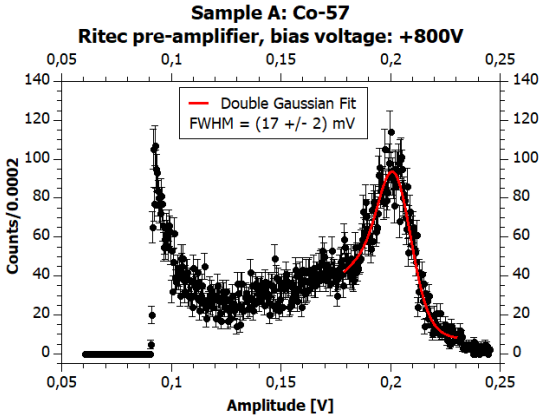

(b) Bias voltage of +800 V.

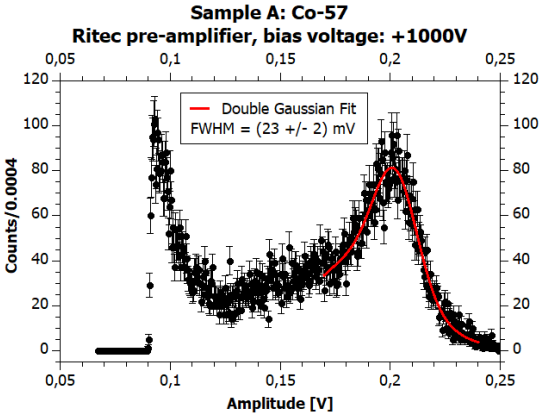

(c) Bias voltage of +1000 V.

Figure 5.15: Plots of measurements with Sample A, when biasing the anode with (a) +600 V, (b) +800 V or (c) +1000 V with Co-57 as irradiation source.

Figure 5.16 puts the three measurements in relation to one another. The 122 keV peaks of

Co-57 are fitted and the FWHM is calculated. The orange error bars show the 95% confidence interval and the turquoise ones the standard deviation. The FWHM results for +600 V and +800 V are close to each other, but all the confidence intervals overlap each other. Including the guard ring might improve the charge collection and the noise level and might yield clearer results, which will be investigated in section 5.4.2.

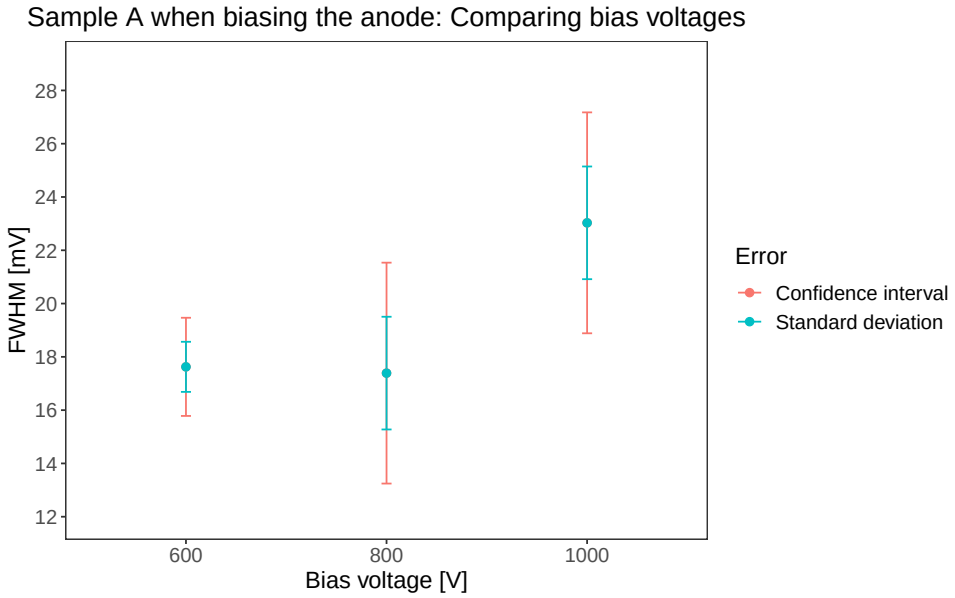

Figure 5.16: Bias voltages at the anode for Sample A at +600 V, +800 V and +1000 V and the corresponding FWHM values of the 122 keV annihilation peak of Co-57. Orange error bars indicate the 95% confidence interval, turquoise error bars represent the standard deviation of the values.

5.4.1.2 Sample B

Sample B is the smaller and thinner detector with only a thickness of 1 mm. Therefore again, a smaller bias voltage is used when biasing the anode. Measurements are performed with Co-57 (electron capture [31]) and values between +300 V and +600 V in 100 V steps. Figure 5.17 shows the spectra and the fitted values of the Full Width at Half Maximum can be found in table 5.8. In all of the spectra the 136.5 keV peak can be distinguished, but it does appear as if it gets more pronounced for +400 V and +600 V. The noise level seems to fluctuate. It should be noted that all spectra show a bump on the left flank of the peak, which is more pronounced for the lower bias voltages. The fit represents these well, which leads to an improved FWHM value. These values should therefore be treated with caution. As with the measurements when biasing the cathode, also here the charge collection should be improved, which might be achievable by including the guard ring.

	+300 V	+400 V	+500 V	+600 V
FWHM ± std	(12 ± 1) mV	(12 ± 5) mV	(24 ± 16) mV	(24 ± 2) mV

Table 5.8: FWHM values of the 122 keV peak of Co-57 in mV for +300 V, +400 V, +500 V and +600 V bias voltage for Sample B when biasing the anode and the corresponding standard deviations.

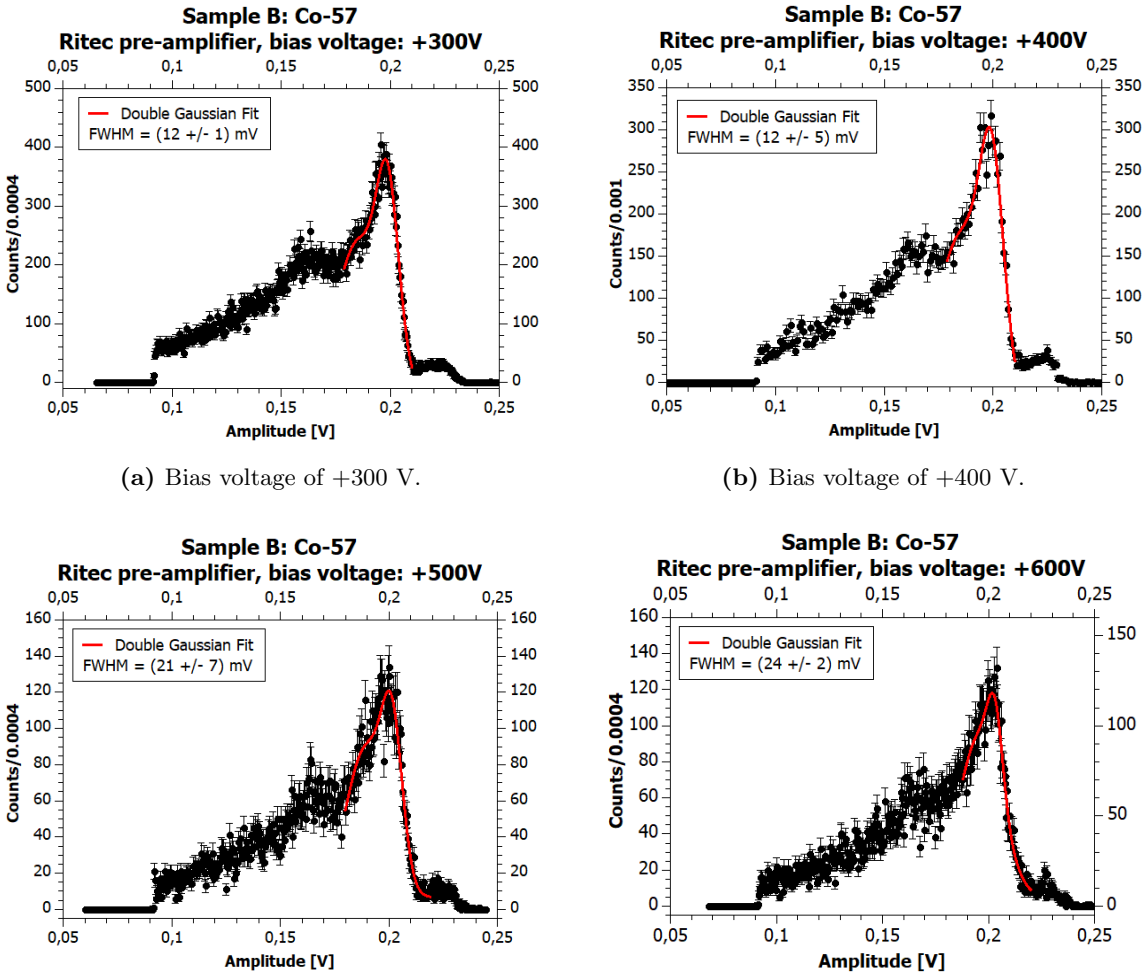

(a) Bias voltage of +300 V.

(b) Bias voltage of +400 V.

(c) Bias voltage of +500 V.

(d) Bias voltage of +600 V.

Figure 5.17: Plots of measurements with Sample B, when biasing the anode with (a) +300 V, (b) +400 V, (c) +500 V or (d) +600 V with Co-57 as irradiation source.

The summary figure 5.18 shows the values of the measurement series in comparison to one another. The orange error bars indicate the 95% confidence interval, the turquoise ones the standard deviation. The error bar for +400 V and +500 V are rather large, making it difficult to state whether a smaller or higher bias voltage is better. A further investigation with the guard ring included will be done in section 5.4.2.

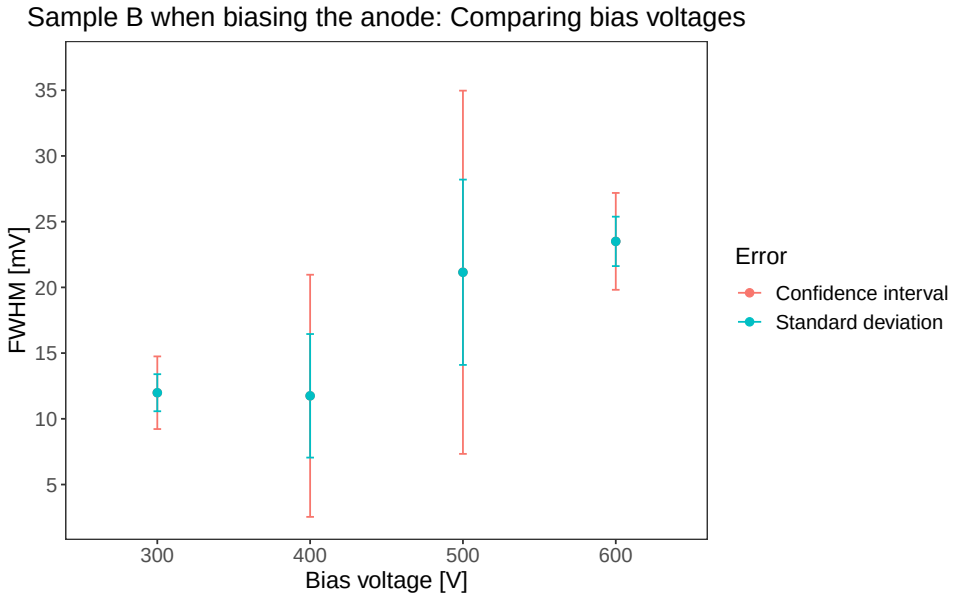

Figure 5.18: Bias voltages at the anode for Sample B at +300 V, +400 V, +500 V and +600 V and the corresponding FWHM values of the 122 keV annihilation peak of Co-57. Orange error bars indicate the 95% confidence interval, turquoise error bars represent the standard deviation of the values.

5.4.1.3 CZT/500

The CZT/500 detector is also connected to the RITEC pre-amplifier PA101C No.804. The settings for the amplifier CAEN Mod. N5688 16CH Spectroscopy Amplifier are a shaping time of 1 μs and a gain of 4. Test measurements with +580, +600 and +620 V are performed with a Na-22 source (β^+-decay [31]) placed (3 $\pm$ 0.1) cm away from the detector. The FWHM at the 511 keV annihilation peak [31] is again determined through fitting and applying the formula (5.1). The results can be seen in figure 5.19 and table 5.9. A comparison between the values is visualized in figure 5.20. The values are higher than for some measurements with Sample A (see e.g. subsection 5.2.1). It should be kept in mind that the Full Width at Half Maximum, as the name suggests, refers to the width at the half maximum. When comparing the spectra of CZT/500 with the ones from Sample A and Sample B, it is obvious that the CZT/500 detector shows a very high resolution. The 511 keV peak (here at around 0.9 V) and the higher peak at 1275 keV (here at around 2.25 V) are not only clearly visible, but further very sharp, thin and high. Also the two compton edges at around 0.6 V and 1.9 V are nicely visible. It should be noted that the higher peak of 1275 keV has not been clearly visible with Sample A in the measurements with Na-22. The charge collection seems by far higher and the noise level a lot lower than for Sample A or Sample B, despite the results of the FWHM.
In figure 5.20 the turquoise error bars indicate the Standard deviation (std) of the fit, the orange error bars the 95% confidence interval. It can be seen that the result for +620 V is the highest, while the FWHM values of +580 V and +600 V lie within each others confidence interval and therefore do not show a statistically difference. It is desirable to have a low FWHM, which is

why +600 V bias voltage is selected for all other measurements.

	+580 V	**+600 V**	**+620 V**
FWHM ± std	(22.6 ± 0.7) mV	(22 ± 1) mV	(31.3 ± 0.9) mV

Table 5.9: FWHM values of the 511 keV annihilation peak of Na-22 in mV for +580 V, +600 V and +620 V bias voltage for the CZT/500 detector and the corresponding standard deviations.

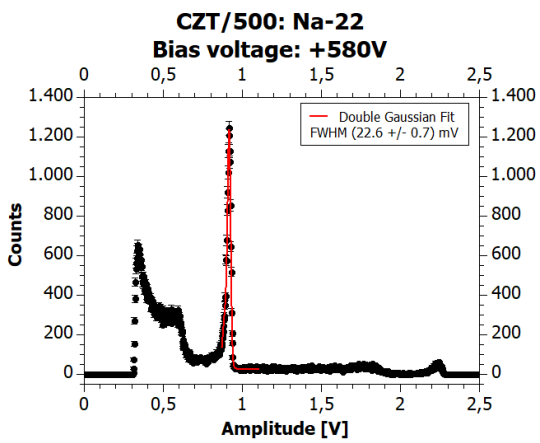

(a) Bias voltage of +580 V.

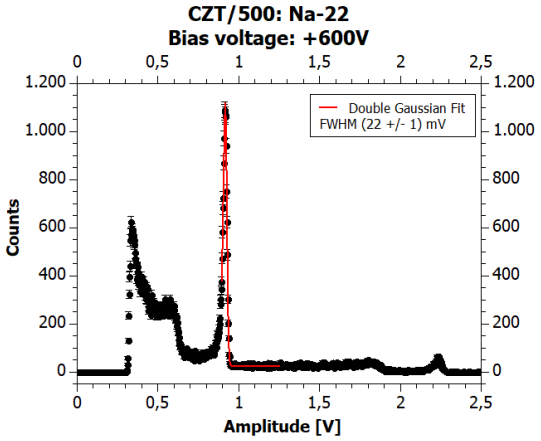

(b) Bias voltage of +600 V.

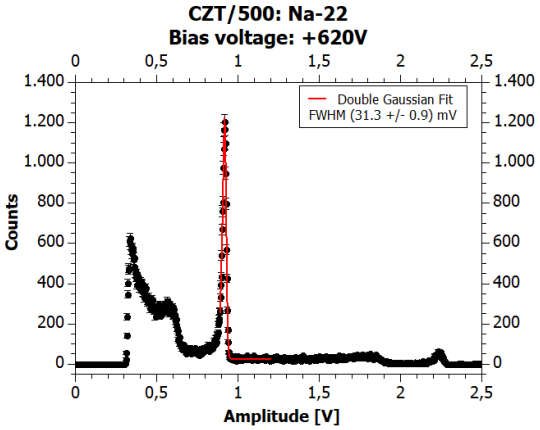

(c) Bias voltage of +620 V.

Figure 5.19: Plots of measurements with the CZT/500 detector, when biasing the anode with (a) +580 V, (b) +600 V or (c) +620 V with Na-22 as irradiation source.

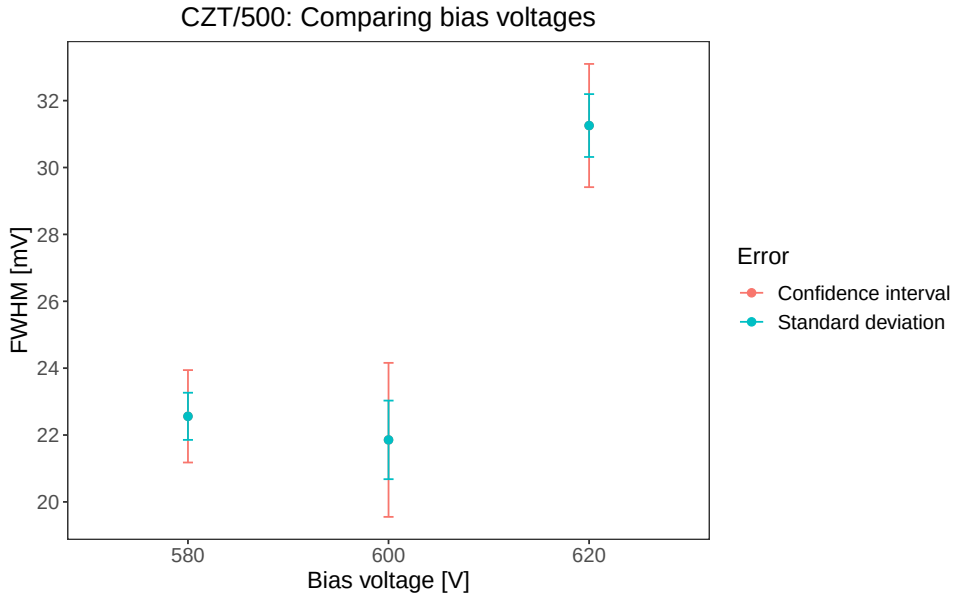

Figure 5.20: Different bias voltages for the CZT/500 detector and the corresponding FWHM values of the 511 keV annihilation peak of Na-22. Orange error bars indicate the 95% confidence interval, turquoise error bars represent the standard deviation of the values for +580 V, +600 V and +620 V.

5.4.2 Including the guard ring

Again, it is possible to improve the charge collection for Sample A and Sample B by including the guard ring. The set up includes the RITEC pre-amplifier PA101C No.804 and the CAEN Mod. N5688 16CH Spectroscopy Amplifier. For the filtering of the high voltage supply for the anode the internal filter of the RITEC pre-amplification structure is used. As the guard ring is now biased as well, a filter with the same values as the internal one is constructed. Figure 5.6 in subsection 5.3.2 gives a visual representation of the HV-filter with resistor values of 100 MΩ for R_{GR1} and 200 MΩ for R_{GR2}, as well as a capacitor value C_{GR} of 220 nF.

5.4.2.1 Sample A

Different positive bias voltages for the anode are tested with various guard ring bias values at a Co-57 source (electron capture [31]). Also the guard ring is biased positively, as the difference between anode and guard ring should not be too large [30], which would be the case if it would be biased negatively. The settings of the amplifier are a shaping time of 1 μs and gain of 5. Positive bias voltages of +500 V to +800 V are tested in 100 V steps. The guard ring values are chosen 10 V below the main bias voltage. For +500 V also a difference of 20 V is tested. Figure 5.21 shows two spectra as examples, namely +500 V with a guard ring bias voltage of +490 V, as well as +800 V with a guard ring voltage of +790 V. The corresponding values are reported in table 5.10. The plots show a high and rather thin peak at the 122 keV position (here at around 0.45 V). In addition, the 136.5 keV peak is clearly distinguishable. This is in stark

contrast to the measurements with biased anode but without the guard ring, as can be seen in the figures in subsection 5.4.1.1.

	bias: +500 V, GR: +490 V	**bias: +800 V, GR: +790 V**
FWHM ± std	(18 ± 1) mV	(19.3 ± 0.7) mV

Table 5.10: FWHM values and the corresponding standard deviations of the 122 keV annihilation peak of Co-57 in mV for +500 V bias voltage and +490 V guard ring (GR) voltage and +800 V bias voltage and +790 V guard ring voltage for Sample A when biasing the anode.

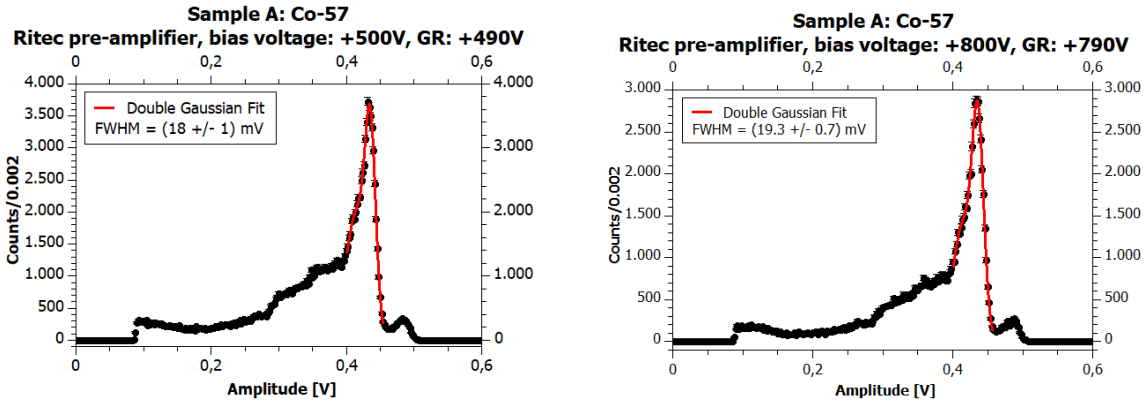

(a) Bias voltage of +500 V and a guard ring bias voltage of +490 V.

(b) Bias voltage of +800 V and a guard ring bias voltage of +790 V.

Figure 5.21: Plots of different bias voltage measurements with Sample A when biasing the anode at (a) +500 V bias voltage and +490 V guard ring (GR) voltage, as well as a bias voltages of (b) +800 V and +790 V guard ring voltage.

The results of the fitted 122 keV Co-57 peak are reported in figure 5.22 for all measurements of the series. Here, the FWHM are shown together with the corresponding 95% confidence intervals (orange) and std error bars (turquoise). The results for the FWHM are very close to each other. In addition, all the error bars are overlapping each other. As it would be expected that higher bias voltages yield better results due to the higher velocity of the charges and the error is the smallest for this value, different guard ring voltages are tested with +800 V.

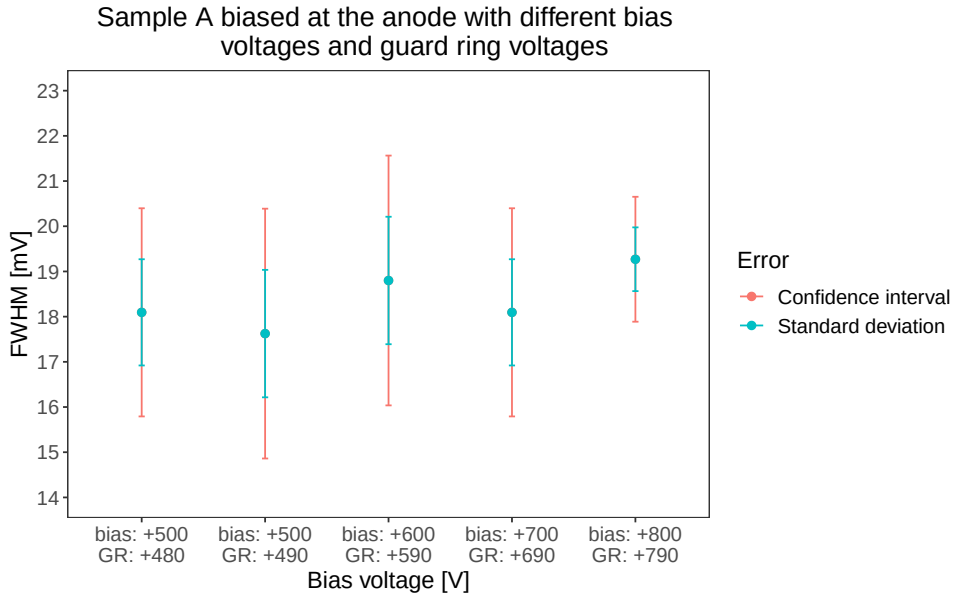

Figure 5.22: Different guard ring bias voltages for Sample A biased at the anode at different bias voltages and the corresponding FWHM values of the 122 keV annihilation peak of Co-57. Orange error bars indicate the 95% confidence interval, turquoise error bars represent the standard deviation of the values.

With a bias voltage of +800 V different guard ring bias voltages are tested, ranging from +740 V to +790 V. Measurements in 10 V steps are performed, as well as a measurement at +785 V to see if there might be an even better result between the two best results of the 10 V step measurements. As an example, two plots are again shown in figure 5.23 and the FWHM values are reported in table 5.11. The 136.5 keV is clearly visible and the 122 keV peak is high and rather sharp.

	+740 V	**+780 V**
FWHM ± std	(24 ± 2) mV	(18.8 ± 0.9) mV

Table 5.11: FWHM values of the 122 keV peak of Co-57 in mV for +800 V bias voltage and +740 V and +780 V guard ring bias voltage for Sample A when biasing the anode and the corresponding standard deviations.

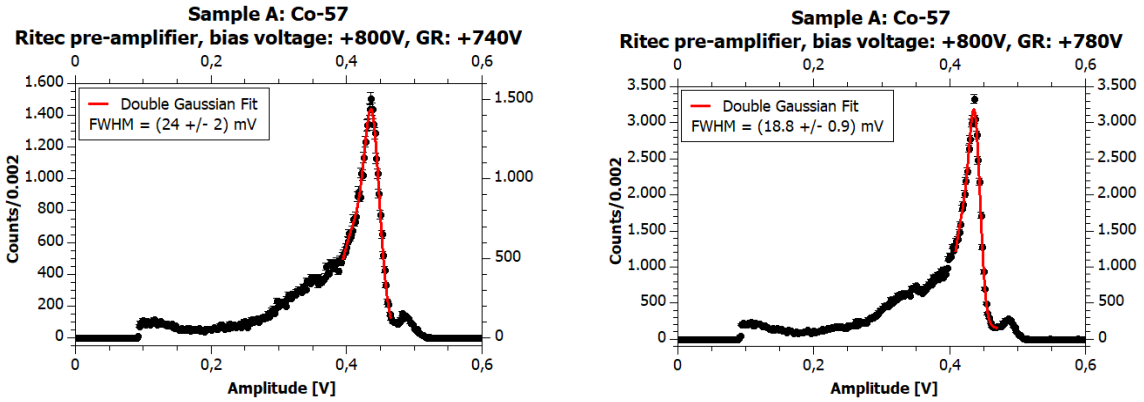

(a) Bias voltage of +800 V and a guard ring bias voltage of+740 V.

(b) Bias voltage of +800 V and a guard ring bias voltage of +780 V.

Figure 5.23: Plots of measurements with Sample A when biased at the anode at (a) +800 V with bias voltages of +740 and (b) +780 V for the guard ring (GR) with Co-57 as irradiation source.

The overview of all measurements and the corresponding error bars can be found in figure 5.24. The orange bars indicate the 95% confidence interval, the turquoise ones the standard deviation. There seems to be a small tendency for improvement with higher bias voltages for the guard ring, meaning a smaller difference between the bias voltage at the anode and at the guard ring.

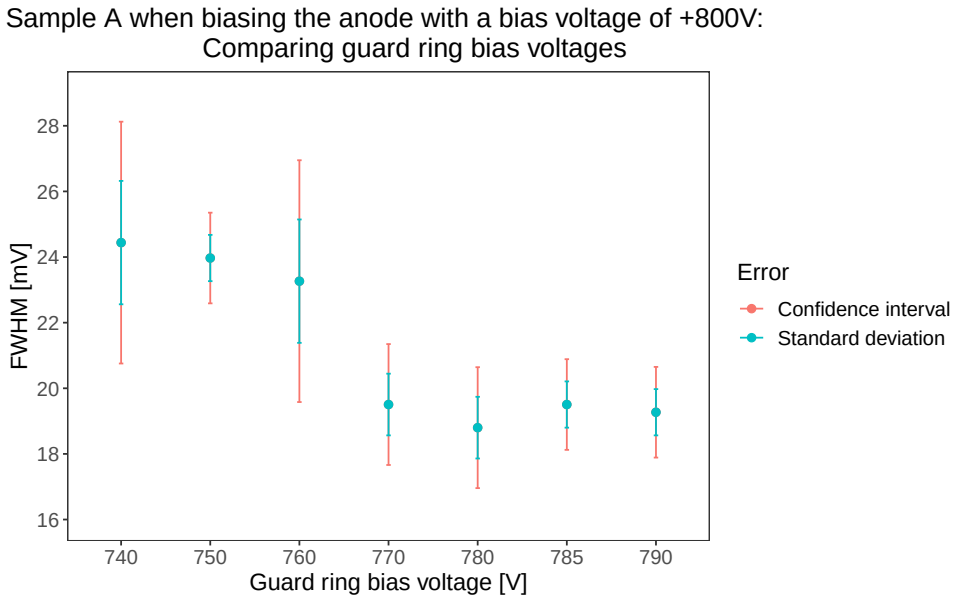

Figure 5.24: Different guard ring bias voltages for Sample A when biasing the anode at +800 V and the corresponding FWHM values of the 122 keV annihilation peak of Co-57. Orange error bars indicate the 95% confidence interval, turquoise error bars represent the standard deviation of the values for measurements between +740 V and +790 V in 10 volt steps, as well as for one measurement at +785 V.

5.4.2.2 Sample B

Different bias voltages for the anode with various guard ring bias voltages are tested. The settings of the amplifier are a shaping time of 1 μs and a gain of 4. The measurements are performed with a Na-22 source (β^+-decay [31]) placed on top of the box in which the detector is located (for a figure of the set up see section 4.2, figure 4.2). Bias voltage values from +300 V to +1000 V are tested with different guard ring voltages. Examples from the measurement series are shown in figure 5.25. These use a bias voltage of +300 V and a guard ring voltage of +280 V, as well as a bias voltage of +900 V and a guard ring of +850 V. The FWHM values are also given in table 5.12. Inspection of the spectra shows that the higher bias voltage also yields a higher peak, which is an indication for a better charge collection. However, in both plots the peak at 1275 keV is not visible. Sample B is too thin and the intrinsic efficiency seems not to be enough for these high energies.

	bias: +300 V, GR: +280 V	**bias: +900 V, GR: +850 V**
FWHM ± std	(68 ± 7) mV	(28 ± 5) mV

Table 5.12: FWHM values and the corresponding standard deviations of the 511 keV annihilation peak of Na-22 in mV for +300 V bias voltage and +280 V guard ring (GR) voltage and +900 V bias voltage and +850 V guard ring voltage for Sample B when biasing the anode.

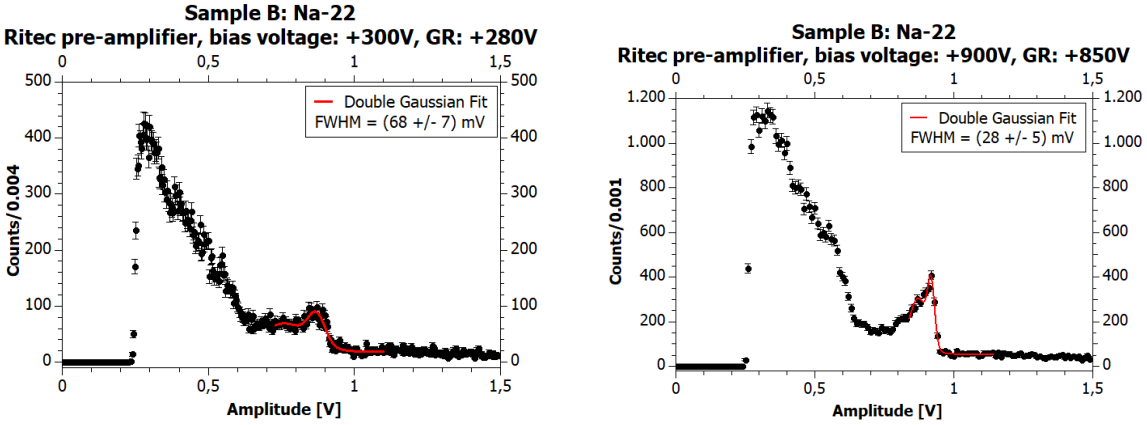

(a) Bias voltage of +300 V and a guard ring bias voltage of +280 V.

(b) Bias voltage of +900 V and a guard ring bias voltage of +850 V.

Figure 5.25: Plots of different bias voltage measurements with Sample B when biasing the anode at (a) +300 V bias voltage and +280 V guard ring (GR) voltage, as well as a bias voltages of (b) +900 V and +850 V guard ring voltage.

The results of the fitted 511 keV Na-22 peak are reported in figure 5.26 for all measurements of the series. The turquoise bars represent the standard deviation, the orange ones the 95% confidence intervals. It seems that there is a tendency for the FWHM value to get smaller with higher bias voltages and guard ring voltages. The influence of the guard ring is further investigated in between the measurement series with a bias voltage of +500 V.

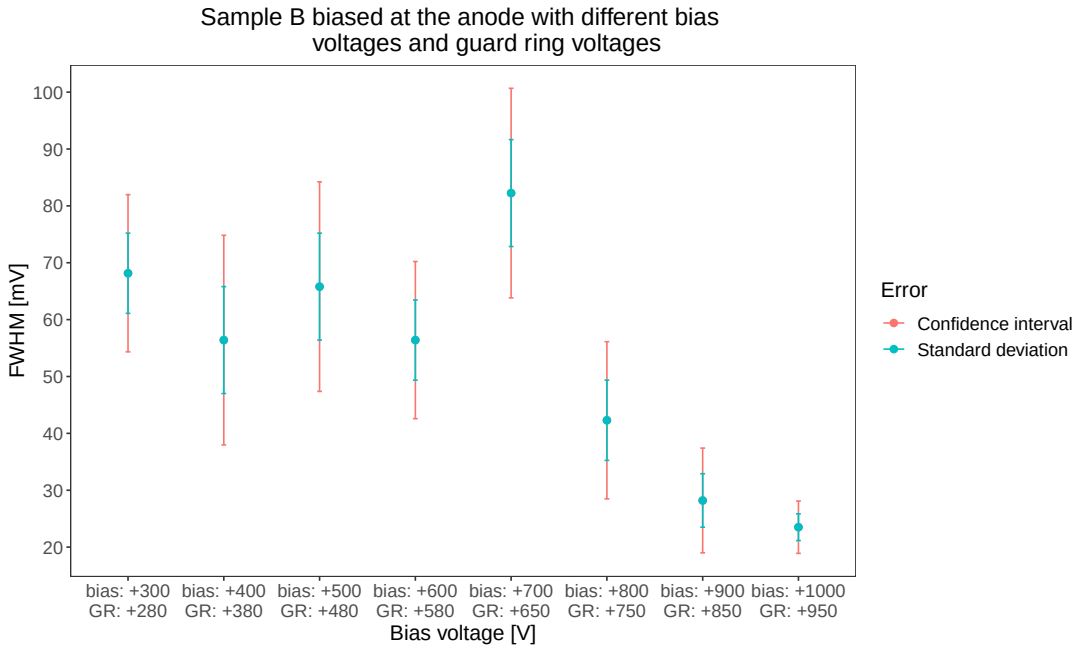

Figure 5.26: Different guard ring (GR) bias voltages for Sample B biased at the anode at different bias voltages and the corresponding FWHM values of the 511 keV annihilation peak of Na-22. Orange error bars indicate the 95% confidence interval, turquoise error bars represent the standard deviation of the values.

In particular, four measurements are done with +500 V bias voltage. This results in a series of measurements with a guard ring bias voltage ranging from +460 V to +490 V in 10 V steps. Figure 5.27 shows two exemplary plots, while table 5.13 gives the corresponding FWHM values. The higher 1275 keV peak is not visible and the 511 keV peak is still small and thick.

	+470 V	**+490 V**
FWHM ± std	(66 ± 9) mV	(101 ± 9) mV

Table 5.13: FWHM values of the 511 keV peak of Na-22 in mV for +500 V bias voltage and +470 V and +490 V guard ring bias voltage for Sample B when biasing the anode and the corresponding standard deviations.

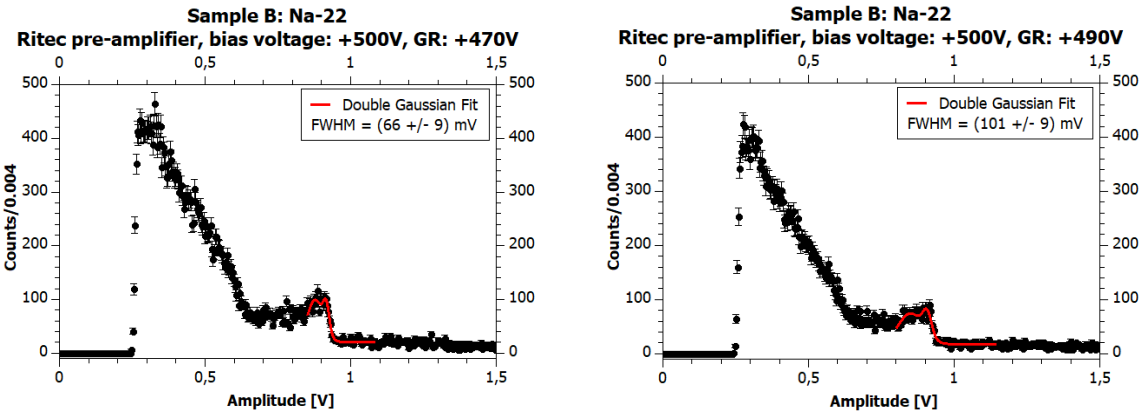

(a) Bias voltage of +500 V and a guard ring bias voltage of+470 V.

(b) Bias voltage of +500 V and a guard ring bias voltage of +490 V.

Figure 5.27: Plots of measurements with Sample B when biased at the anode at (a) +500 V with bias voltages of +470 and (b) +490 V for the guard ring (GR) with Na-22 as irradiation source.

The overview of all measurements and the corresponding error bars can be found in figure 5.28, with orange error bars as indication for the 95% confidence interval and turquoise bars as standard deviations. In general, the FWHM values are quite large and also show a large error. One could conclude that a very small difference between bias voltage (+500 V) and guard ring voltage (+490 V) seems to yield the worst result. However, a clear tendency of guard ring bias voltage is not extractable.

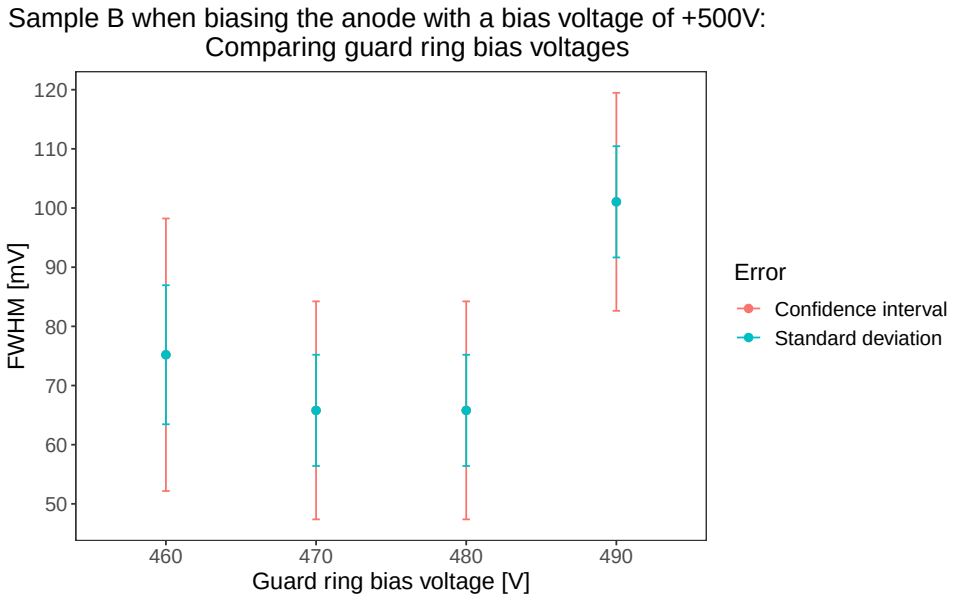

Figure 5.28: Different guard ring bias voltages for Sample B when biasing the anode with +500 V and the corresponding FWHM values of the 511 keV annihilation peak of Na-22. Orange error bars indicate the 95% confidence interval, turquoise error bars represent the standard deviation of the values for measurements between +460 V and +490 V in 10 volt steps.

5.5 Energy calibration

It would be desirable to be able to perform an energy calibration of the detector. To do so, different sources with known peaks need to be measured first with the exact same settings for each measurement. The peaks of interest are fitted and from this the corresponding amplitude values/x-coordinates can be extracted. The relationship between these values can then be calculated by fitting a linear function, which gives a slope that can be used to convert amplitude values (in V) to energy values (in keV). Now, another irradiation source can be measured with the same set up and the amplitude values converted to energies. If the peak energy values are known, it can be checked whether the energy calibration was successful. An energy calibration is done in the following for the CZT/500 detector and Sample A, but not Sample B, as Sample B is too thin for the available sources.

5.5.1 CZT/500

First an energy calibration is performed for the CZT/500 detector. This is used as a benchmark to determine if the same testing is doable to perform with Sample A. Should an energy calibration not be feasible with the CZT/500 detector, despite the great results of resolution achieved, a calibration with Sample A is unrealistic. For the energy calibration, energy spectra of three different irradiation sources, namely Na-22 (β^+-decay), Co-57 (electron capture), as well as Co-60 (β^--decay) [31] are taken. All measurements are performed with the same settings for the amplifier, which is a shaping time of 1 μs and a gain of 4. The characteristic peaks of the sources are fitted and the corresponding x-position values extracted. These indicate which amplitude value corresponds to the highest point of the peak. The values can be reviewed in table 5.14. Figure 5.29 shows a graphical representation of the values for all sources. The red line indicates the linear fit which yields an R^2 of 0.99, indicating an almost linear relationship. The estimated energy calibration factor is the slope of the linear fit. Due to the excellent results, an energy calibration of measurement results with the CZT/500 is feasible.

	Energy peak	**Amplitude/x-location value**
Na-22	511 keV	(0.9132 ± 0.0007) V
	1275 keV	(2.227 ± 0.001) V
Co-57	122 keV	(0.20868 ± 0.00006) V
	136.5 keV	(0.23345 ± 0.00008) V
Co-60	1173 keV	(2.016 ± 0.002) V
	1333 keV	(2.311 ± 0.004) V

Table 5.14: Values of the characteristic energy peaks of the sources Na-22, Co-57 and Co-60. The corresponding amplitude/x-position values are determined by fitting the relevant peaks of measurements with the CZT/500 detector.

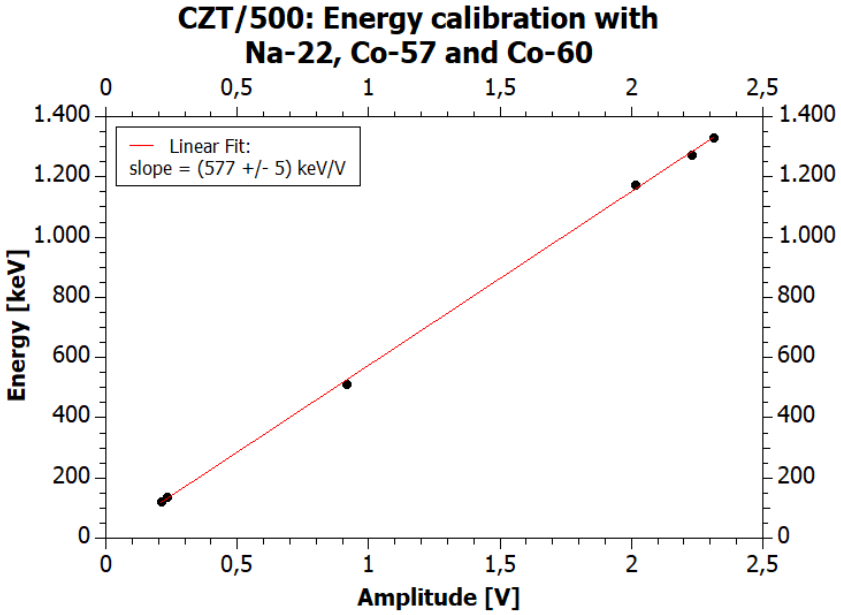

Figure 5.29: Results of energy calibration with the CZT/500 detector. The x-axis represents the measured amplitude values (extracted by fitting the characteristic energy peaks), the y-axis the characteristic energy peaks. The red line indicates the linear fit with an R^2 of 0.99 and a slope of (577 ± 5) keV/V.

A radium pointer of an old watch is measured with the same settings to test the energy calibration and the performance of the CZT/500. Figure 5.30 shows the measurement with a calibrated x-axis. The peaks are fitted with a Gaussian distribution. Even though the true values are not within the error range of the fitted values, the results are close to the assumed energy peaks of a Ra-226 source [31] and the measurement can be deemed successful. A comparison of the Ra-226 energy peaks and the measured values can be found in table 5.15.

	Energy peak	**Measured values**
Ra-226	186 keV	(184.2 ± 0.3) keV
	242 keV	(235.7 ± 0.5) keV
	295 keV	(289.6 ± 0.3) keV
	352 keV	(344.6 ± 0.3) keV
	609 keV	(599.5 ± 0.8) keV

Table 5.15: Values of the characteristic energy peaks of Ra-226. The corresponding measured values are determined by fitting the relevant peaks of measurements with the CZT/500 detector.

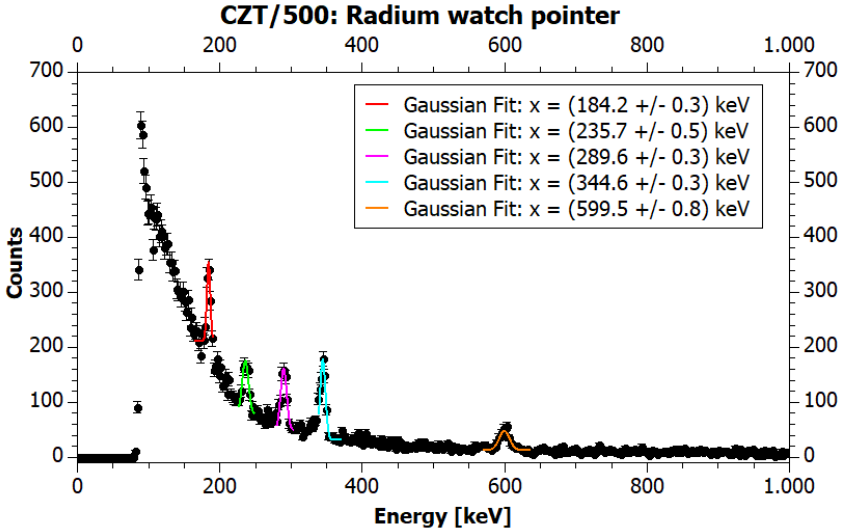

Figure 5.30: Spectrum of a radium pointer of an old watch with the CZT/500 detector. The x-axis represents the measured values in keV based on the energy calibration. The characteristic Ra-226 peaks are fitted.

5.5.2 Sample A

Measurements with a Na-22 source (β^+-decay) and a Co-57 source (electron capture) [31] are performed with Sample A with a bias voltage of +500 V and a guard ring voltage of +480 V. It is possible to fit the 511 keV for the Na-22 source, however, the 1275 keV peak is not clear enough to be fitted. For the Co-57 source both peaks at 122 keV and 136.5 keV are fitted. The settings for the amplifier are the same for all measurements, namely a shaping time of 1 μs and a gain of 5. The fitted and extracted values are reported in table 5.16. These indicate which amplitude value corresponds to the highest point of the peak. The linear relationship between the values is presented in figure 5.31. The red line is the linear fit which yields an R^2 of 0.99, indicating a close to perfect linear relationship. However, this value needs to be treated with caution, as only three peaks are used for establishing the energy calibration.

	Energy peak	**Amplitude/x-location value**
Na-22	511 keV	(1.781 ± 0.004) V
Co-57	122 keV	(0.418 ± 0.002) V
	136.5 keV	(0.473 ± 0.005) V

Table 5.16: Values of the characteristic energy peaks of the sources Na-22 (only the 511 keV is fitted) and Co-57. The corresponding amplitude/x-position values are determined by fitting the relevant peaks of measurements with Sample A.

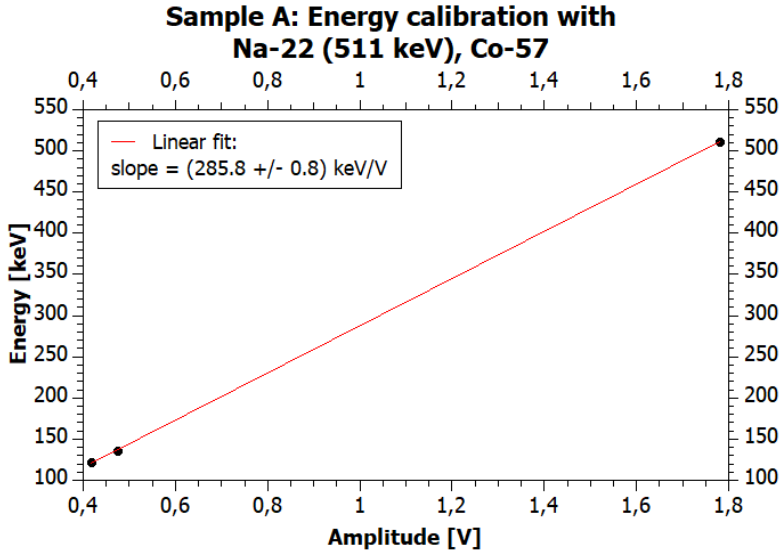

Figure 5.31: Results of energy calibration with Sample A. The x-axis represents the measured amplitude values (extracted by fitting the characteristic energy peaks) and the y-axis the characteristic energy peaks. The red line indicates the linear fit with an R^2 of 0.99 and a slope of (285.8 ± 0.8) keV/V.

5.6 Foil measurements

As Sample B is thinner, it should be more sensitive to lower energies than Sample A. Therefore, measurements with foils of different elements with lower energies are performed with it and with the CZT/500 detector for comparison. For both detectors the RITEC pre-amplifier and the internal HV-filter are used. The settings of the amplifier are a shaping time of 1 μs and a gain of 4. In order to be able to excite the material, a Sr-90 source (e^--emitter[31]) is used. Depending on the measurement, different material is placed on top of the detector. On top of any material the Sr-90 source is placed. The emitted electrons are then able to excite the underlying material and the detector can measure the signal. Figure 5.32 shows some of the used foils. On the bottom one can see lead (Pb), in the middle to the left tin (Sn) and to the right Molybdenum-Rhenium (MoRe). In addition to the depicted foils, silver (Ag) foils are used, as well as plastic layers for shielding purposes.

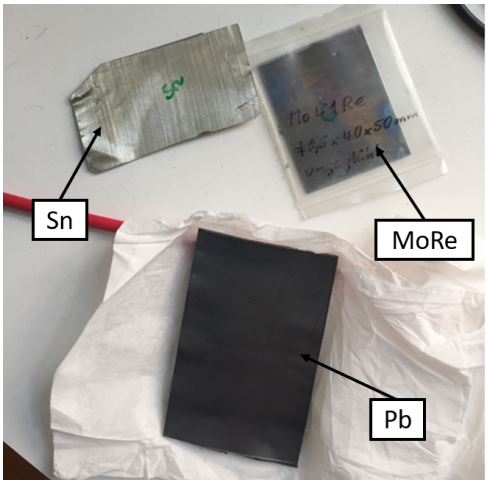

Figure 5.32: Some of the foils used for the measurements. At the bottom is a layer of lead (Pb), in the middle to the left tin (Sn) and to the right Molybdenum-Rhenium (MoRe). The foil on the top of the picture is not used.

5.6.1 Sample B

A positive bias voltage of +1000 V at the anode is used for Sample B. The same filter as for the previous measurements is used for the guard ring bias voltage of +950 V. The corresponding filter circuit can be seen in subsection 5.3.2 in figure 5.6. Sample B is again placed in the metallic box (see figure 4.2) with the lid closed. The different material is placed on the lid and on top of this the Sr-90 source. The order in which the foils are reported in the titles of the plots always state the foil closest to the Sr-90 source first. For an impression, a schematic of a specific set up is given in figure 5.33 (a). Figure 5.33 (b) shows a picture of the real set up for another of the measurements. All the other set ups can be pictured in a similar way. No real energy calibration could be performed for Sample B, however, the fitted value at the 511 keV peak of the measurement with the same settings of +1000 V bias voltage and +950 V guard ring bias voltage can be used as an estimate for the calibration value. As the 511 keV peak for this measurement yields an amplitude of (920.8 ± 0.9) mV, the factor for converting measured amplitude to keV can be calculated as in section 5.5 by dividing 511 keV by 920.8 mV, yielding a factor of around 554.95 $\frac{\text{keV}}{\text{V}}$. This value is used in the measurements with Sample B to convert the x-axis values to keV.

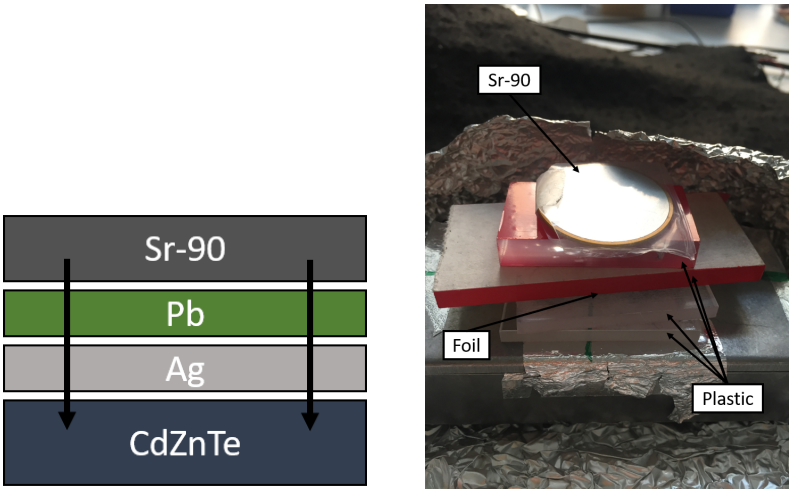

(a) Schematic set up with Sample B for one specific measurement.

(b) Actual set up with Sample B for another specific measurement.

Figure 5.33: The set up with Sample B for the measurements with different foils. (a) shows a schematic representation with Pb and Ag, (b) shows an actual set up with plastic and a foil. In both, the detector and the Sr-90 source can be seen.

A lead (Pb) foil (1 mm) is used for the first series of measurements. First, only Pb is used, resulting in figure 5.34 (a). The peak for lead is clearly visible and it is even possible to distinguish the $K_{\alpha 1}$- and the $K_{\beta 1}$-line. They are respectively at 75 keV and 85 keV [32]. The corresponding fitted energy values for Sample B are reported in table 5.17.
Figure 5.34 (b) shows a measurement with lead (Pb) (1 mm) and tin (Sn) (0.1 mm). The peak for tin is expected at 25.3 keV, which is still within the noise peak in this measurement. The lead cannot shield off the electrons emitted from the Sr-90 enough. When comparing (a) and (b) in figure 5.34 one can see that the lead peak does decrease through the addition of foils of tin and is not so precise either. In subplot (c) of the same figure, a thicker tin layer (0.15 mm) and a plastic layer are included. The Sn-line is still not visible. Also increasing the plastic to 6 or 9 mm does not improve the result.
Only when the lead is replaced by another layer of plastic right after the Sr-90 source does the Sn peak appear. It is still rather hidden in the noise peak, but one can tell them apart, as can be seen in figure 5.34 (d). The fitted values and the corresponding known values are reported in table 5.17. The values are close to the known parameters.

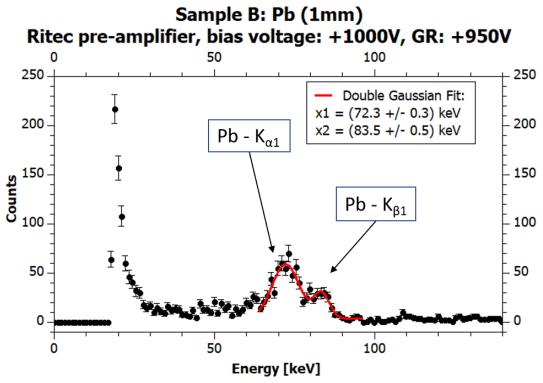

(a) Pb (1 mm).

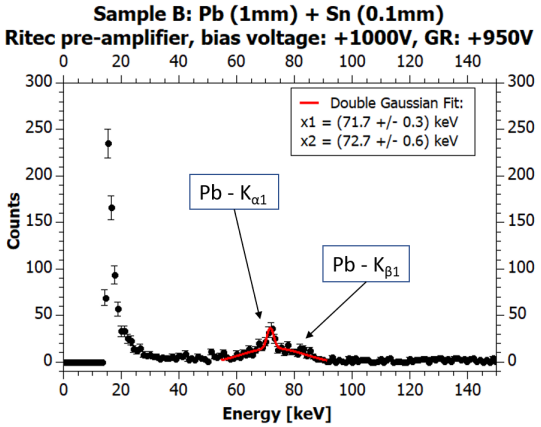

(b) Pb (1 mm) + Sn (0.1 mm).

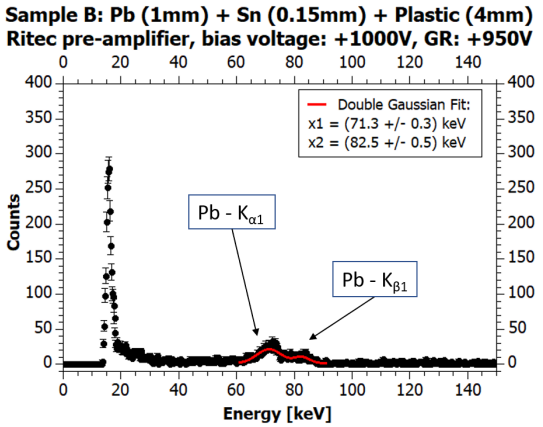

(c) Pb (1 mm) + Sn (0.15 mm) + Plastic (4 mm).

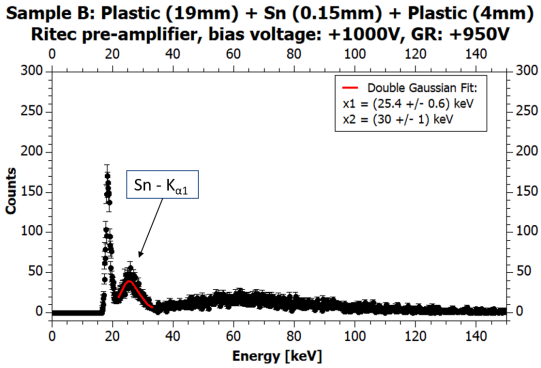

(d) Plastic (19 mm) + Sn (0.15 mm) + Plastic (4 mm).

Figure 5.34: Plots of measurements with Sample B and Sr-90 as an irradiation source with (a) Pb (1 mm), (b) Pb (1 mm) + Sn (0.1 mm), (c) Pb (1 mm) + Sn (0.15 mm) + Plastic (4 mm) and (d) Plastic (19 mm) + Sn (0.15 mm) + Plastic (4 mm).

		Energy peak	Measured values
Pb	$K_{\alpha 1}$	75 keV	(72.3 ± 0.3) keV
	$K_{\beta 1}$	85 keV	(83.5 ± 0.5) keV
Sn	$K_{\alpha 1}$	25.3 keV	(25.4 ± 0.6) keV
	$K_{\beta 1}$	28.5 keV	(30 ± 1) keV

Table 5.17: Values of the characteristic energy peaks of Pb and Sn. The corresponding measured values are determined by fitting the relevant peaks of measurements with Sample B.

Another set of measurements is carried out with Molybdenum-Rhenium (MoRe) and tin (Sn). Figure 5.35 reports the results of the different set ups. (a) shows a measurement with a layer of MoRe (0.5 mm) and one of tin (0.15 mm). Only the peak corresponding to Re can be seen

and fitted, as Mo has its main peak at 17.5 keV [32], which is too low and still covered in the noise peak. Figure 5.35 (b) is the same set up with an additional layer of plastic (6 mm) in order to shield additional electrons which cover the tin peak. However, the Sn peak is not visible and still covered in the noise peak. Subfigure (c) is the same set up with a thicker plastic of 9 mm. Here, the tin peak starts to be visible and distinguishable from the noise peak and can be fitted, while the Mo peak is still not visible. Table 5.18 shows the results of the fitted peaks of measurement (c) and the corresponding known peaks for the materials. They are quite close to the expected values.

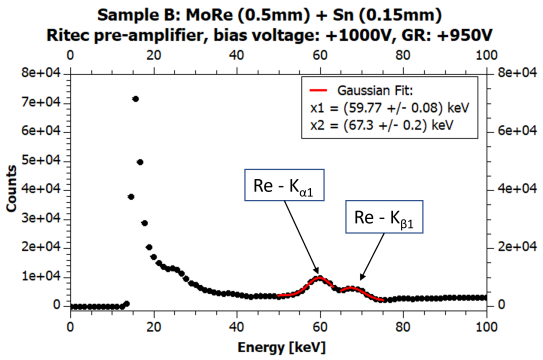

(a) MoRe (0.5 mm) + Sn (0.15 mm).

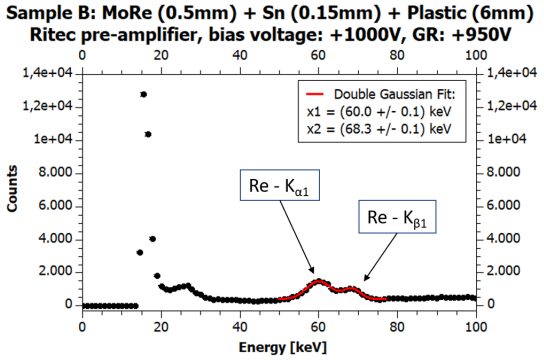

(b) MoRe (0.5 mm) + Sn (0.15 mm) + Plastic (6 mm).

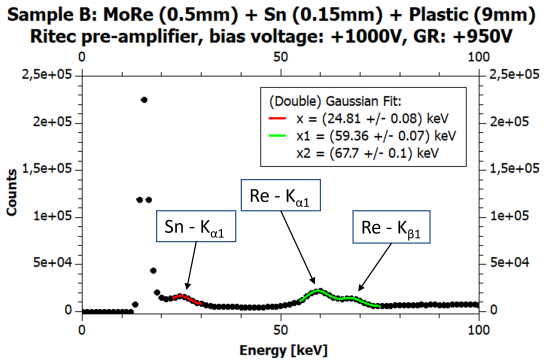

(c) MoRe (0.5 mm) + Sn (0.15 mm) + Plastic (9 mm).

Figure 5.35: Plots of measurements with Sample B and Sr-90 as an irradiation source with (a) MoRe (0.5 mm) + Sn (0.15 mm), (b) MoRe (0.5 mm) + Sn (0.15 mm) + Plastic (6 mm) and (c) MoRe (0.5 mm) + Sn (0.15 mm) + Plastic (9 mm).

		Energy peak	Measured values
Re	$K_{\alpha 1}$	61.1 keV	(59.36 ± 0.07) keV
	$K_{\beta 1}$	69.3 keV	(67.7 ± 0.1) keV
Sn	$K_{\alpha 1}$	25.3 keV	(24.81 ± 0.08) keV

Table 5.18: Values of the characteristic energy peaks of MoRe and Sn. The corresponding measured values are determined by fitting the relevant peaks of measurements with Sample B.

In addition, measurements with silver (Ag) are performed. Figure 5.36 (a) shows a measurement with lead and 0.1 mm of silver (Ag). The silver peak should be at 22.2 keV, however this value is still covered in the noise peak and further shielding is needed to see the peak.
Figure 5.36 (b) shows the measured spectrum when shielding the electrons from the Sr-90 source off with plastic. For this, first a thicker layer of plastic is placed, then a larger layer of Ag (0.2 mm) and then plastic again. Now, the Ag peak is visible. The $K_{\alpha 1}$ peak should be located at 22.2 keV, and the $K_{\beta 1}$-line at 24.9 keV [32]. The fitted values can also be seen in table 5.19. They are very close to the known values.

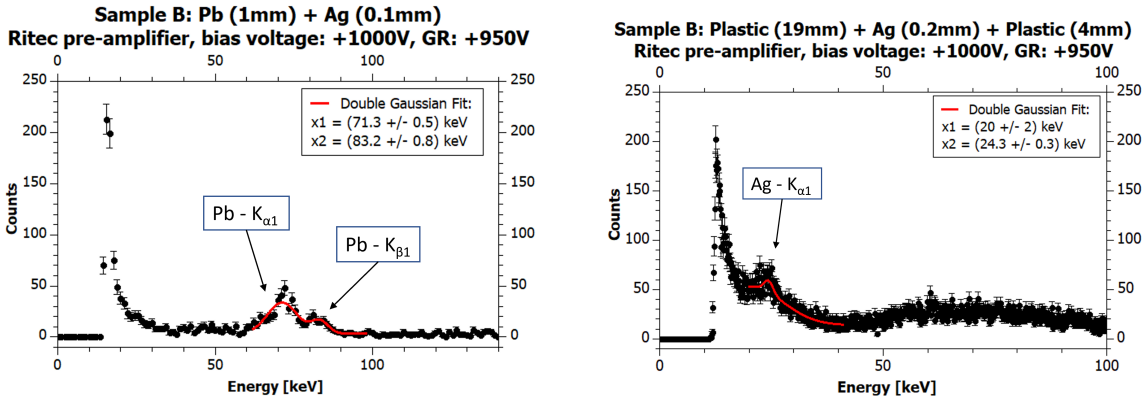

(a) Pb (1 mm) + Ag (0.1 mm).

(b) Plastic (19 mm) + Ag (0.2 mm) + Plastic (4 mm).

Figure 5.36: Plots of measurements with Sample B and Sr-90 as an irradiation source with (a) Pb (1 mm) + Ag (0.1 mm) and (b) Plastic (19 mm) + Ag (0.2 mm) + Plastic (4 mm).

		Energy peak	Measured values
Ag	$K_{\alpha 1}$	22.2 keV	(20 ± 2) keV
	$K_{\beta 1}$	24.9 keV	(24.3 ± 0.3) keV

Table 5.19: Values of the characteristic energy peaks of Ag. The corresponding measured values are determined by fitting the relevant peaks of measurements with Sample B.

When comparing the known energy peaks of the materials and the measured values, one can see that they lie close to each other. Sample B is able to measure Pb nicely, as well as Sn and Ag with extra shielding.

5.6.2 CZT/500

The CZT/500 is biased with +600 V. Again Sr-90 is used as an irradiation source. The foils are placed right after the source at a distance to the detector. The order in which the foils are reported in the titles of the plots always state the foil closest to the Sr-90 source first. The energy calibration extracted in subsection 5.5.1 is used to convert the amplitude values to keV. Figure 5.37 shows measurements with MoRe (0.5 mm), plastic and silver (0.2 mm). In subfigure (a) a thicker layer of plastic is placed between MoRe and Ag, while (b) shows the results of a set up where a thicker layer of plastic is placed right before the detector. For subfigure (c) plastic is only placed right before the detector.

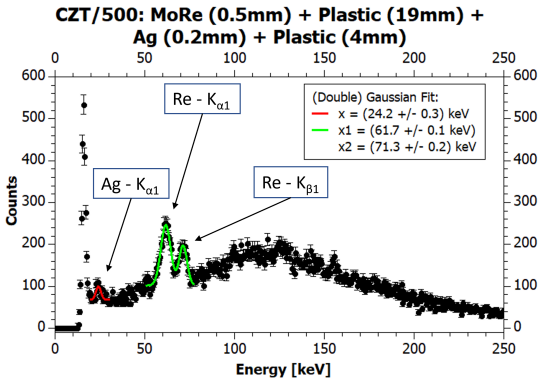

(a) MoRe (0.5 mm) + Plastic (19 mm) + Ag (0.2 mm) + Plastic (4 mm).

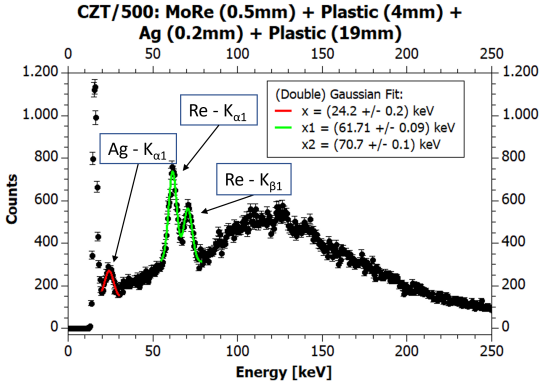

(b) MoRe (0.5 mm) + Plastic (4 mm) + Ag (0.2 mm) + Plastic (19 mm).

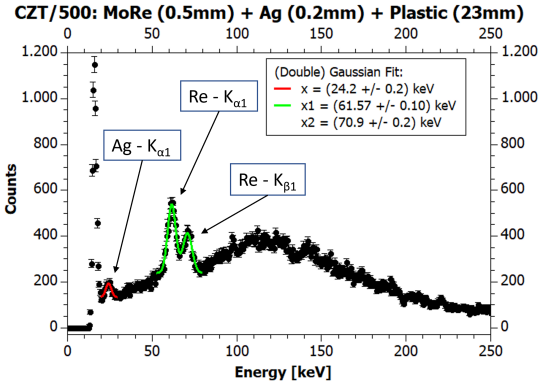

(c) MoRe (0.5 mm) + Ag (0.2 mm) + Plastic (23 mm).

Figure 5.37: Plots of measurements with CZT/500 and Sr-90 as an irradiation source with (a) MoRe (0.5 mm) + Plastic (19 mm) + Ag (0.2 mm) + Plastic (4 mm), (b) MoRe (0.5 mm) + Plastic (4 mm) + Ag (0.2 mm) + Plastic (19 mm) and (c) MoRe (0.5 mm) + Ag (0.2 mm) + Plastic (23 mm).

Table 5.20 reports on the extracted values of figure (b).

		Energy peak	**Measured values**
Re	$K_{\alpha 1}$	61.1 keV	(61.71 ± 0.09) keV
	$K_{\beta 1}$	69.3 keV	(70.7 ± 0.1) keV
Ag	$K_{\beta 1}$	24.9 keV	(24.2 ± 0.2) keV

Table 5.20: Values of the characteristic energy peaks of MoRe and Ag. The corresponding measured values are determined by fitting the relevant peaks of measurements with CZT/500.

The CZT/500 detector is also able to measure values of Re and go down as low as to the peak of Ag.

6 Conclusion and outlook

The characterization measurements of Sample A and Sample B yield interesting results.
Using the AMPTEK pre-amplifier with Sample A yields rather noisy results. Even when including the guard ring, the noise level is still too high. However, the measurements with the RITEC pre-amplifier show clearly that the charge collection improves when including the guard ring. This could be shown for both biasing the cathode and the anode. From this it can be concluded that a large improvement was achieved by switching from the AMPTEK pre-amplifier to the RITEC pre-amplifier and by including the guard ring, suggesting that these two, the pre-amplifier and the guard ring, are the main noise sources.
In general, measurements when biasing the anode yield better results. This is probably due to the fact that the internal HV-filter of the RITEC pre-amplifier was used, which is less susceptible to pick up external noise than the one used when biasing the cathode.
Measurements with Sample B yield higher FWHM results and more noise in the spectra than Sample A. This is due to the lower quality of Sample B. It has a larger area and is thinner, which results in a lower intrinsic efficiency.
A general tendency of better performance with higher bias voltage can be extracted. However, whether a higher or lower guard ring bias voltage improves the results more, cannot be established.

The energy calibration showed that the CZT/500 detector is able to detect and correctly assign different Ra-226 energy peaks of an old radium watch pointer. It was not possible to perform the same energy calibration with Sample A successfully, as not all peaks could be detected and the extracted values showed a systematic shift. This is probably due to the higher noise level for Sample A, which needs to be improved further for a successful energy calibration.

While the CZT/500 detector is able to detect also the high 1275 keV peak of Na-22, Sample A is not able to report on this with the current set up.
Sample B is able to detect the energy peaks of different materials, such as Pb (75 keV) or Re (61.1 keV). Even more, it is able to go to energies as low as Sn (25.3 keV) and Ag (22.2 keV).
The CZT/500 detector is also able to detect peaks of Re (61.1 keV) and Ag (22.2 keV).

Future measurements could look into the effect of temperature on the noise level by cooling the set up. This might yield interesting insights into how well Sample A's energy resolution can be improved, which might be able to see the higher Na-22 energy peak due to its thickness. In addition, Sample B might be able to detect even lower energy regions.

Abbreviations

Ag Silver. 57, 61–63

ASTRA Advanced ultra-fast solid STate detectors for high precision RAdiation spectroscopy. 1, 3

Au Gold. 6

Cd Cadmium. 3, 6

CdTe Cadmium Telluride. 1, 3, 4, 6, 21

CdZnTe Cadmium Zinc Telluride. 1, 3–9, 13–15, 21, 56

CT Cadmium Telluride. 1

CZT Cadmium Zinc Telluride. 1, 16

FWHM Full Width at Half Maximum. 1, 25, 27, 29–31, 33–52, 63

Ge Germanium. 3–5

HPB High-Pressure Bridgman. 6, 7

HV High Voltage. 19–21, 25, 26, 31, 32, 46, 57, 63

Mo Molybdenum. 57, 59–61

Pb Lead. 57, 58, 61, 63

Pl Platinum. 6

Re Rhenium. 57, 59, 61–63

Si Silicium. 3–5

Sn Tin. 57–61, 63

std Standard deviation. 27, 33–38, 41, 43–45, 47, 48, 50, 51

Te Tellurium. 3, 6

Z Atomic number. 3

Zn Zinc. 3, 6

List of Figures

List of Tables

Bibliography

[1] STRONG-2020. Online. http://www.strong-2020.eu/. Accessed: 24th of October 2020.

[2] Zmeskal Johann. ASTRA. Workshop H2020 European Inegrating Initiative in Hadron Physics, October 2017.

[3] Takahashi Tadayuki and Watanabe Shin. Recent Progress in CdTe and CdZnTe Detectors. *IEEE Transactions on Nuclear Science*, 48(4):950–959, August 2001.

[4] Del Sordo Stefano, Abbene Leonardo, Caroli Ezio, Mancini Anna Maria, Zappettini Andrea, and Ubertini Pietro. Progress in the Development of CdTe and CdZnTe Semiconductor Radiation Detectors for Astrophysical and Medical Applications. *Sensors*, 9:3491–3526, 2009. doi:10.3390/s90503491.

[5] Min Jiahua, Shi Zhubin, Qian Yongbiao, Sang Wenbin, Zhao Hengyu, Teng Jianyong, and Liu Jishan. Simulation of the anode structure for capacitive Frisch grid CdZnTe detectors. *Nuclear Science and Techniques*, 20:46–50, 2009.

[6] CIAAW. Standard Atomic Weights. Online. https://ciaaw.org/atomic-weights.htm. Accessed: 25th of October, 2020.

[7] Zmeskal Johann. Detector and detector systems for particle and nuclear physics 1 - Part 1. Lecture at the University of Vienna, 2016.

[8] Gross Rudolf and Marx Achim. *Festkörperphysik*. De Gruyter, Berlin/Boston, 3rd edition, 2018.

[9] Kittel C. *Introduction to Solid State Physic*. John Wiley, New York, 6th edition, 1986.

[10] Guo Si-Ming, Wu Jin-Jie, Zhang Jian, Li Xu-Fang, Lju Cong-Zhan, Zhang Shuai, Li Cheng-Ze, Bin-Bin Huo, and Liao Zhen-Qu. Study on temperature coefficient of CdTe detector used for X-rays detection. *Chinese Physics C*, 2016.

[11] Zappettini A. and Bettelli M. Report. Technical report, Istituto Materiali per Elettronica e Magnetismo (IMEM) - CNR, Parma, Italy, 2020.

[12] Abbene Leonardo, Principato Fabio, Gerardi Gaetano, Bettelli Manuele, Seller Paul, Veale Matthew C., Nicola Zambelli, Benassi Giacomo, and Zappettini Andrea. Digital fast pulse shape and height analysis on cadmium-zin-telluride arrays for high-flux energy-resolved X-ray imaging. *Journal of synchrotron radiation*, 25:257–271, 2018.

[13] Alineason. Bridgman technique. Online. https://www.alineason.com/en/knowhow/crystal-growth/. Accessed: 25th of October 2020.

[14] Institute for Single Crystals. Bridgman. Online. http://iscrystals.com/page-catalog.html?cat_id=86. Accessed: 26th of October 2020.

[15] Heffelfinge J.R., Medlin D.L., and James R.B. Analysis of grain boundaries, twin boundaries and precipitates in $Cd_{1-x}Zn_xTe$ grown by High-Pressure Bridgman method. pages 247–252. Materials Research Society, 1997. doi:10.1557/PROC-484-247.

[16] ZRF Ritec Sia, Riga, Latvia. *Large Volume Hemispherical Nuclear Radiation Detector Model CZT/500 - User Manual.*

[17] Zappettini Andrea. PCB and detector layout. Technical report.

[18] Zappettini Andrea. Information on Sample A & Sample B. Technical report.

[19] Pristauz-Telsnigg Doris. Technical drawings, September 2020.

[20] Scordo Alessandro. Characterization of the X + Gamma detectors. Technical report.

[21] Cremat Inc. Advice in using cremat CSP modules. Online, 2020. https://www.cremat.com/applications/csp-application-notes/. Accessed: 28th of August, 2020.

[22] Schröder Heinrich. *Elektrische Nachrichtentechnik 1. Band - Grundlagen, Theorie und Berechnung passiver bertragungsnetzwerke*, volume 1. Verlag für Radio-Foto-Kinotechnik GmbH, Berlin, 1973.

[23] Amptek Inc., 14 DeAngelo Drive, Bedford, MA, USA. *PC250 Test Board for the A250.*

[24] ZRF Ritec Sia, Riga, Latvia. *Miniature Preamplifier Model PA1010C Model PA1010C/HV - User Manual.*

[25] C.A.E.N. *Technical Information Manual Mod. N968 Spectroscopy Amplifier*, 8th edition, July 2016.

[26] Wikipedia.com. Full width at half maximum. Online. https://en.wikipedia.org/wiki/Full_width_at_half_maximum. Accessed: 8th of June, 2021.

[27] IONDEV SRL. *QtiPlot - Data Analysis and Scientific Visualisation.* IONDEV SRL, Bucuresti, Romania, 2011.

[28] R Core Team. *R: A Language and Environment for Statistical Computing.* R Foundation for Statistical Computing, Vienna, Austria, 2020.

[29] RStudio Team. *RStudio: Integrated Development Environment for R.* RStudio, PBC., Boston, MA, 2020.

[30] Zmeskal Johann. Private communication.

[31] ld didactic.de. Radioaktive Quellen. Online. https://www.ld-didactic.de/software/524221de/Content/Appendix/RadioactiveSources.htm. Accessed: 2nd of April, 2021.

[32] Thompson Albert, Lindau Infolf, Attwood David, Liu Yanwei, Eric Gullikson, Pianetta Piero, Howells Malcolm, Robinson Arthur, Kim Kwang-Je, Scofield James, Kirz Janos, Underwood James, Kortright Jeffrey, Williams Gwyn, and Winick Herman. *X-ray data booklet*. Larence Berkeley National Laboratory, University of California, Berkeley, CA 94720, 3rd edition, 2009.